

AN ABSTRACT OF THE THESIS OF

Chaojiao Sun for the degree of Doctor of Philosophy in Oceanography presented on September 24, 1997.

Title:

Dynamic Instability of Stratified Shear Flow in the Upper Equatorial Pacific.

Abstract approved: _____ **Redacted for privacy** _____

James N. Moum

The hypothesis that stratified shear flow instability is responsible for the maintenance of the deep cycle of turbulence immediately below the mixed layer and above the core of the Equatorial Undercurrent (EUC) in the Pacific, is examined by means of linear stability analysis. The 3-dimensional Taylor-Goldstein equation is solved numerically, using observed currents and stratification from the Tropical Instability Waves Experiment. A diurnal cycle in the growth rate of shear instability is found, similar to that of the deep-cycle turbulence. Multiple unstable modes exist, each associated with different critical levels. The kinetic energy extracted from the mean flow is redistributed away from the critical level, providing a source for the vertical flux of momentum downward through the EUC. Wavelength and propagation direction of unstable modes from this linear stability analysis agree reasonably with those estimated from concurrent observations.

The parameter dependence of unstable modes upon external background background variables is investigated, using linear stability solutions of more than 120 background profiles. The goal is to diagnose shear instability from the background conditions without solving the eigenvalue problem explicitly. The growth rate is

rate is shown to be approximately proportional to the reduced shear ($S - 2N$, where $S^2 = U_z^2 + V_z^2$, $N^2 = -g\bar{\rho}_z/\rho_0$) evaluated at the critical level. The critical level of an unstable mode is almost perfectly correlated with the depth of the nearest local maximum of reduced shear (or minimum of the gradient Richardson number, Ri). The direction of propagation of unstable modes approximately follows the direction of maximum shear, i.e., along or against the direction of shear vector, at its critical level. The wavelength may be estimated from the radius of curvature of reduced shear at the critical level.

Dynamic Instability of Stratified Shear Flow in the Upper Equatorial Pacific

by

Chaojiao Sun

A THESIS

submitted to

Oregon State University

in partial fulfillment of
the requirements for the
degree of

Doctor of Philosophy

Presented September 24, 1997

Commencement June 1998

Doctor of Philosophy thesis of Chaojiao Sun presented on September 24, 1997

APPROVED:

Redacted for privacy

Major Professor, representing Oceanography

Redacted for privacy

Dean of the College of Oceanic and Atmospheric Sciences

Redacted for privacy

Dean of the Graduate School

I understand that my thesis will become part of the permanent collection of Oregon State University libraries. My signature below authorizes release of my thesis to any reader upon request.

Redacted for privacy

Chaojiao Sun, Author

ACKNOWLEDGMENT

I am indebted to my major advisor Jim Moum for his invaluable guidance and unwavering support throughout my graduate study. His work on equatorial turbulence, along with that of others, inspired me to explore the role of shear instability in the mixing of stratified fluid. Jim has always challenged and encouraged me to pursue new ideas. His hard-working and fun-loving have been inspirational. I am very grateful to him for his understanding, patience and friendship over the years.

I thank Bill Smyth for being an invaluable member of my committee. He has made important contributions to every aspect of my professional development. His insight and enthusiasm has been an inspiration to this work. His advice, from doing research to writing papers, from giving seminars to writing resume, has been tremendously beneficial to me. His friendship and sense of humor are also greatly appreciated.

I am very grateful to other members of my committee for their encouragement and support. This study originated from a class project when John Allen taught the "dynamic instability" course. He has been helpful and encouraging and offered enlightening and constructive comments during the progress of this project. Murray Levine has always been helpful and supportive and readily available for discussions. I thank T. Darrah Thomas for his willingness to serve on my committee. He kindly stayed on the committee even after his retirement from OSU. His help and encouragement is much appreciated.

My thanks are extended to many teachers and colleagues. Clayton Paulson acted as a co-advisor during the first year of my study here. His kind help and understanding throughout these years are greatly appreciated. Eric Kunze provided

a thorough and constructive review for chapter 2. I enjoyed stimulating discussions with Eric D'Asaro. Discussions with Doug Caldwell, Tom Sanford, Mike McPhaden, Roland DeSzoke, Charlie Erickson, Dave Hebert, Hementha Wijesekera, Laurie Padman, Priscilla Newberger, Ren-Chieh Lien and Darek Bogucki are helpful. Alison McDonald provided me with warm support and helpful advice, ranging from thesis defense to job seeking. Help and support from Ed Llewellyn, Ray Kreth, Mike Neely-Brown, Mike Zelman, Eric Beals, Tom Leach, Chuck Sears, Andy Dale and Cindy Withrow are much appreciated. Enrich Thomann and Satish Reddy of the Department of Mathematics of OSU kindly discussed with me about mathematical techniques used or considered in this study. I am grateful to Tom Dierrich of the Department of Computer Science of OSU for his helpful career advice and encouragement.

I am indebted to the foreign student advisors of the Office of International Education of OSU for much helpful advice. Especially, Dr. William Smart has helped me enormously since the first day of my arrival at OSU. His professionalism and compassion will always be warmly remembered in my heart. I am grateful to the head student advisor Irma Delson of COAS for her sound advice and warm encouragement during critical times. I thank Donna Obert, Jeff Gonor and Robin Hlobeczy of Student Services of COAS for their help.

I thank my fellow graduate students for their support and friendship over the years. Here is an incomplete list: Ayal Anis, Alberto Mestas-Núñez, Dylan Righi, Scott Pegau, Yunda Yao, Shusheng Luan, Hongbo Qi, Xiaoqing Li, Ed Zaron, Robin Robertson, Jonathan Nash, Gunnar Gunderson, Sheila O'Keefe, Donna Witter, Susan Howard, Kieran O'Driscoll, Eric Antonissen, Kipp Shearman, Lynn Berkery, Jose Bettencourt, Shanji Zhang, Vassilis Zvakis, Jorge Mesias, Tony Martinez, John Lyman, Julie Pullen and Ivana Cerovecki. I thank my officemates Ayal Anis,

Jonathan Nash and Gunnar Gunderson for warm support, helpful discussions and interesting conversations. I thank Jonathan for helpful tips about LaTeX. Friends, teachers, and colleagues I have not specifically mentioned, thank you all for your support.

Many wonderful friends has made my life more enjoyable and meaningful. Bo and I shared numerous hiking and camping trips to the many wondrous national parks and beautiful coasts of Oregon and Washington with Ding Rugang and his wife Lian Song, Guibiao Lin and his wife Chen Yang, Yunda Yao and his wife Gelian Cai. Many delightful weekend gatherings with them are remembered with fondness. Hongyan Li has been a wonderful friend since I first came to Corvallis. We had a good time hanging out, going to the movies, cooking and shopping together. I enjoyed many holidays and gatherings with Pat, Bob Collier and Mary Mooney. I first met Pat and Mary on board R/V Wecoma in 1991. Their friendship has been an important part of my wonderful experience here in the beautiful Oregon. Kate Zhang has been a best friend since the COARE experiment in 1992. Chun Zhu and Yatao Hu have been a great friend since our days in college. I thank Baiyun Ran and her husband Xiaodong Xu, Shusheng Luan and his wife Yanong Tan, Hongbo Qi and his wife Pei Wu, Xiaoqing Li and his wife Yueqiu Wang for their friendship and kind help.

Last but not the least, I am indebted to my parents, my sister and brother for their love and expectations. I thank Bo Huang for being a best friend and a firm supporter. I could not have done it without his love, thoughtfulness, patience and courage.

The surface current mooring data were obtained from Michael McPhaden of NOAA Pacific Marine Environmental Laboratory. This work was funded by the National Science Foundation (OCE-8816098 and OCE-9314396).

CONTRIBUTION OF AUTHORS

Drs. William D. Smyth and James N. Moum were involved in the design, analysis and writing of each manuscript.

TABLE OF CONTENTS

	<u>Page</u>
1 GENERAL INTRODUCTION	1
2 DYNAMIC INSTABILITY OF STRATIFIED SHEAR FLOW IN THE UPPER CENTRAL EQUATORIAL PACIFIC	4
2.1 Introduction	5
2.2 Background conditions	7
2.2.1 The data	7
2.2.2 Basic state for the linear stability analysis	8
2.3 The eigenvalue problem	13
2.4 Numerical method	14
2.4.1 Data processing	14
2.4.2 Range of wavenumbers	16
2.4.3 Initial guesses for the eigenvalue	17
2.5 Detailed study of unstable modes from a single hour	17
2.5.1 Mean profiles during hour 6	17
2.5.2 The dispersion relation	19
2.5.3 Vertical structure of unstable modes	24
2.6 Variability of shear instability over a 24-hour period	28
2.7 Comparison with related studies	31
2.7.1 Concurrent observations of internal waves	31
2.7.2 Internal waves observed during Tropic Heat 2	34
2.7.3 Theoretical studies	35
2.8 Summary	36

TABLE OF CONTENTS (Continued)

	<u>Page</u>
3 PARAMETER DEPENDENCE OF SHEAR INSTABILITY UPON BACKGROUND VARIABLES: RESULTS FROM LINEAR STABILITY ANALYSIS	38
3.1 Introduction.....	39
3.2 Background conditions.....	40
3.3 Variability of shear instability and deep cycle of turbulence.....	45
3.3.1 Variability of shear instability over 5 days.....	45
3.3.2 Variability of the deep cycle of turbulence.....	48
3.4 Parameter dependence of instability.....	52
3.4.1 What determines the location of critical level?	52
3.4.2 What determines the growth rate?	54
3.4.3 What determines the propagation direction?.....	61
3.4.4 What determines the wavelength?.....	63
3.5 Conclusions	65
4 GENERAL CONCLUSIONS	67
BIBLIOGRAPHY	70
APPENDICES	73
APPENDIX A Derivation of 3-D Taylor-Goldstein equation	74
APPENDIX B The radiation boundary condition and its effects.....	76

LIST OF FIGURES

<u>Figure</u>	<u>Page</u>
2.1 (a) Time series of temperature at 35 m from two thermistors deployed over the side of the ship, one at the bow and one aft. The data shown were obtained on day 313, 1991 at 0°N, 140°W during TIWE. The two time series are offset by 0.1°. (b) Surface wind stress τ (N m^{-2}) (c) Surface buoyancy flux J_b (W kg^{-1}) (d) Logarithm of hourly averaged turbulent kinetic energy dissipation rate ϵ ($\text{m}^2 \text{s}^{-3}$) for the same time period.	9
2.2 Hourly averaged (a) zonal, (b) meridional velocity, (c) logarithm of total shear squared $\log_{10} S^2$ on the same day as in Fig. 2.1.	10
2.3 Hourly averaged (a) logarithm of buoyancy frequency squared $\log_{10} N^2$ (b) inverse gradient Richardson number Ri^{-1} and (c) reduced shear $S - 2N$ on the same day as in Fig. 2.1.	11
2.4 Background profiles of hour 6 on year day 313. (a) zonal velocity U , (b) meridional velocity V , (c) total shear squared $U_z^2 + V_z^2$ and zonal shear squared U_z^2 . The meridional shear squared is represented by the shaded region. (d) buoyancy frequency squared N^2 , (e) $S - 2N$ (f) Ri^{-1}	18
2.5 Growth rate and critical level versus zonal and meridional wavenumbers k (10^{-2} rad/m) and l (10^{-2} rad/m).	20
2.6 Contour plots of growth rate and critical level versus zonal and meridional wavenumbers, k and l , for the background conditions of hour 6 on day 313.	21
2.7 Eigenfunctions of the dominant mode of each of the three families of unstable modes present at hour 6.	25
2.8 Growth rates ω_i ($\times 10^{-4} \text{s}^{-1}$) versus critical levels of all unstable modes superimposed on profiles of background quantities. (a) U (solid line) and V (dashed line), (b) S^2 , (c) U_{zz} (solid line) and V_{zz} (dashed line), (d) N^2 , (e) $S - 2N$, (f) Ri^{-1}	26
2.9 (a) Hourly averaged buoyancy flux J_b on day 313. (b) Growth rate of the unstable modes of each hour. (c) Image and contours of the zonal velocity. (d) Reduced shear $S - 2N$	29

LIST OF FIGURES (Continued)

<u>Figure</u>	<u>Page</u>
2.10 (a) Same as Fig. 2.9a. The phase velocities of mode 1, 2, 3 and 4 are shown in (b), (c), (d) and (e), respectively. (f) The frequency of unstable modes seen by a stationary observer. (g) The wavelengths of unstable modes.	30
3.1 Hourly averaged (a) zonal (b) meridional velocity from day 311 to 315.	41
3.2 Squared hourly averaged (a) zonal shear (U_z^2) (b) meridional shear (V_z^2) (c) total shear ($U_z^2 + V_z^2$) from day 311 to 315. The thick black line denotes the base of the surface mixed layer.	43
3.3 Hourly averaged (a) squared buoyancy frequency (N^2) (b) Inverse Richardson number (c) $S - 2N$ from day 311 to 315.	44
3.4 (a) Contours of zonal velocity U and (b) Reduced shear $S - 2N$	46
3.5 Time series of (a) wind stress τ and (b) buoyancy flux J_b (c) growth rates of unstable modes ω_i	47
3.6 (a) Growth rates ω_i versus the Eulerian frequencies ω_r of unstable modes in the earth's frame. (b) Growth rates ω_i versus the wavelengths λ of the unstable modes.	49
3.7 (a) wind stress τ . (b) buoyancy flux J_b . (c) Hourly averaged turbulent kinetic energy dissipation rate ϵ	50
3.8 (a) Time series of growth rates. (b) Hourly averaged $\log_{10} \langle \epsilon \rangle$	51
3.9 (a) Critical level depth (z_c) versus the depth of local Richardson number minimum (z_{Ri}). (b) Critical level depth (z_c) versus the depth of local $S - 2N$ maximum (z_{S-2N}).	53
3.10 (a) The depth of local Richardson number minimum (z_{Ri}) versus the depth of local $S - 2N$ maximum (z_{S-2N}). (b) Growth rate normalized by the shear at its critical level versus the Richardson number at the critical level.	55
3.11 (a) Normalized growth rate ω_i/S versus \sqrt{Ri} evaluated at the critical level. (b) Growth rate ω_i versus $(S - 2N)/4$ evaluated at the critical level.	56

LIST OF FIGURES (Continued)

<u>Figure</u>	<u>Page</u>
3.12 (a) ω_i/S vs. \sqrt{Ri} for the <i>tanh</i> , <i>sin</i> and <i>sech</i> ² functions, which corresponds to the prototypes of smooth shear layer, channel flow and Bickley jet. (b) $\omega_i/(S - 2N)$ vs. <i>Fr</i> for the same set of functions as in (a).	58
3.13 (a) $\omega_i/(S - 2N)$ vs. <i>Ri</i> for <i>tanh</i> , <i>sin</i> and <i>sech</i> functions, which correspond to the prototypes of smooth shear layer, channel flow and Bickley jet. (b) ω_i/S vs. $(S - 2N)/(4S)$	60
3.14 (a) Direction of unstable modes versus the direction of maximum shear at the critical level (144 modes). (b) Same as in (a) except only for modes with growth rates $\omega_i > 10^{-4}s^{-1}$	62
3.15 (a) Wavelengths of unstable modes λ versus R_{S-2N} , the radius of curvature of $S - 2N$ at the critical level. (b) Wavelengths λ versus R_{Ri} , the radius of curvature of <i>Ri</i> at the critical level.	64

List of Tables

<u>Table</u>		<u>Page</u>
2.1	Parameters of the fastest growing modes of three mode families of hour 6 during day 313	23
2.2	Parameters of the shallowest unstable mode from hour 5 to hour 9 during day 313 for comparison with observations	33

LIST OF APPENDICES

<u>Appendix</u>		<u>Page</u>
A	Derivation of 3-D Taylor–Goldstein equation	74
B	The radiation boundary condition and its effects	76

DEDICATION

To
my parents
and
in loving memory of
grandma

DYNAMIC INSTABILITY OF STRATIFIED SHEAR FLOW IN THE UPPER EQUATORIAL PACIFIC

1 GENERAL INTRODUCTION

During the Tropic Heat experiments in the central Equatorial Pacific in 1984, the most intriguing finding is the discovery of the so-called "deep-cycle turbulence" (Moum and Caldwell, 1985; Gregg *et al.*, 1985). Turbulence increased by at least an order of magnitude at night in the stratified region between the base of the mixed layer and the core of the Equatorial Undercurrent (EUC).

The generation mechanism of this deep-cycle turbulence is not obvious. A hypothesis was that it was forced by internal gravity waves. In a further experiment (Tropic Heat 2) in 1987, evidence of high-frequency waves in the deep-cycle region was observed and its link to the deep cycle turbulence was confirmed (For a summary, see Moum *et al.*, 1992a). But the nature of these high-frequency waves could not be identified. They could be internal gravity waves generated at the base of mixed layer. These waves could traveled downward into the stratified region, broke down and generated turbulence. Or these observed waves could be locally generated shear instability waves. This hypothesis is based on the fact that the gradient Richardson number Ri ($= N^2/S^2$, N is the buoyancy frequency, $N^2 = -g\bar{\rho}_z/\rho_0$, S is the total vertical shear of current, $S^2 = U_z^2 + V_z^2$) was near its critical value $1/4$ for instability in the deep cycle region. The clear correlation between high-frequency waves and

strong mixing was further reinforced by observations during part of the Tropical Instability Wave Experiment (TIWE) in 1991 (Lien *et al.* , 1996).

Our goal is to test the hypothesis that shear stability could be one of the mechanisms for the maintenance of the deep cycle of turbulence by means of linear stability analysis. Linear stability theory involves an initial value problem in a steady flow. We chose hourly-averaged measurements during TIWE as the input for the stability problem .

Instability of the initial flow field permits small-scale billows to grow exponentially until they reach finite amplitude. They then develop secondary instabilities and become turbulent. The Fourier components of the small disturbances are referred to as “modes”. The intensity of instability generation is represented by the growth rates of unstable modes.

The criterion $Ri < 1/4$ is a necessary but insufficient condition for linear instability. Attempts to find a critical value of Ri for the onset of instability have been unsuccessful so far. To find out whether a particular background condition is stable or not, the stability problem—a complex eigenvalue problem has to be solved. Since analytical solutions are only achievable for very few special function forms, most of the problems must be solved numerically.

Our objective is to solve the stability problem with complicated profiles measured from the ocean, so that we may find out

- Are oceanic conditions favorable to shear instability generation? If so, is there a diurnal cycle in the growth rates of shear instability?
- Through what mechanism is shear instability generated in the real ocean?
- Can instability waves penetrate into deep ocean?

The challenges we are facing to solve this problem are:

- To model the ocean conditions using measurements to retain complex information about the flow field, yet without unnecessary, interfering details which may result in numerical instability.

- To develop a numerical method to solve this stability problem.
- To analyze and interpret the numerical solutions.
- To investigate the parameter dependence of shear instability upon background variables.

In the first paper (Chapter 2), we developed a numerical method to solve the stability problem with our measurements. Hourly-averaged profiles were used as the background conditions. The stability problem was solved for a 24-hour period. We find that the flow field was favorable to the generation of shear instability at night. The highest growth rates were up to $2.1 \times 10^{-3} \text{ s}^{-1}$. So the instability waves can increase its magnitude to $e = 2.718$ times in less than 8 minutes. It is shown that an unstable mode extracts energy from the mean at its critical level and redistributes the energy away from the critical level into other regions.

In the second paper (Chapter 3), we extended our stability analysis to five continuous days of data and found a clear diurnal cycle in the growth rates of shear instability. This diurnal cycle corresponded with the diurnal variability in the observed wave activity and turbulent kinetic energy dissipation rates. We also studied the statistics of the parameters of unstable modes and investigated their relationship with the parameters of background profiles. The goal is to be able to evaluate the potential importance of shear instability for a given background condition without numerically solving the stability problem. The background reduced shear $S - 2N$ is shown to be an important parameter in predicting the growth rate of instability.

**2 DYNAMIC INSTABILITY OF STRATIFIED SHEAR FLOW IN
THE UPPER CENTRAL EQUATORIAL PACIFIC**

Chaojiao Sun, William D. Smyth and James N. Moum
Oregon State University

Submitted to *Journal of Geophysical Research*,
July 11, 1997.

2.1 Introduction

Shear instability has been suggested as a possible source of turbulent mixing in the stratified region above the Equatorial Undercurrent (EUC) core. A diurnal cycle in the turbulent kinetic energy dissipation rate, both in and below the surface mixed layer, was discovered during the Tropic Heat experiment [Moum and Caldwell, 1985; Gregg *et al.*, 1985]. Intermittent bursts of intense turbulence were observed during nighttime in the stratified, low gradient Richardson number (Ri) shear zone between the base of the mixed layer and the Equatorial Undercurrent (EUC) core [Peters *et al.*, 1988; Moum *et al.*, 1989]. The cause of the so-called “deep-cycle” turbulence was not known. It was speculated that locally generated internal waves could be responsible for stimulating these bursts in the thermocline. In a further experiment, Tropic Heat 2, evidence of high-frequency, wavelike signals was found in the high shear zone [see Moum *et al.*, 1992a for a review] from both towed thermistor-chain observations [Moum *et al.*, 1992b] and temperature time series from a mooring [McPhaden and Peters, 1992]. Microstructure measurements taken simultaneously with the towed thermistor observations showed the existence of turbulent overturns associated with packets of wavelike activity [Hebert *et al.*, 1992]. The possible mechanisms for the observed wave signals were suggested as either downward traveling internal waves generated at the base of the mixed layer, the so-called “obstacle effect”, or locally-generated shear instability waves [e.g., Wijesekera and Dillon, 1991]. Although observed gradient Richardson numbers did not drop below the critical value $1/4$, Mack and Hebert [1997] have suggested that strong, near-surface shear, which was not properly resolved by the shipboard current profiler, could have reduced the Richardson number and led to shear instability.

Our present knowledge of shear instability comes primarily from theoretical analyses and laboratory studies, which usually address simple flow geometries. In contrast, measurements from the ocean reveal complex structures of current and stratification. While linear stability theory assures stability when Ri is everywhere greater than $1/4$ in the flow [*Miles*, 1961; *Howard*, 1961], the onset of instability depends in a subtle way on the details of the velocity and density profiles [e.g., *Howard and Maslowe*, 1973]. Analytical solutions are only achievable for very few special functions [e.g. *Drazin and Howard*, 1966; *Lott et al.*, 1992]. *Hazel* [1972] was the first to solve the problem numerically for a set of analytical functions. Subsequently, many authors have solved the stability problem with various analytical functions [e.g., *Davis and Peltier*, 1976; *Smyth and Peltier*, 1989; *Winters and Riley*, 1992; *Sutherland et al.*, 1992]. *Sutherland* [1996] studied the shear instability problem for the upper flank of the EUC using simple analytical functions to represent the background profiles.

As part of the Tropical Instability Wave Experiment (TIWE), an extensive data set including simultaneous measurements of microstructure, current and internal waves was collected. Ri calculated from the measurements frequently fell below $1/4$ below the mixed layer [*Lien et al.*, 1995]. This provided us an excellent opportunity to study the shear instability problem with measured background conditions. The objective of this paper is to investigate the characteristics of shear instability under realistic ocean conditions by solving the linear stability problem numerically, using background profiles derived from measurements during TIWE.

We introduce the background condition for our analysis in Section 2. In section 3, we provide a brief introduction to linear instability theory and present the eigenvalue problem we solve. Numerical method is presented in Section 4. In section 5, the unstable modes for one single hour are examined in detail. This is

followed in Section 6 with a survey of the solutions over a 24-hour period. In Section 7, we compare the characteristics of unstable modes from this analysis with related studies, including concurrent observations of internal waves, similar observations made during Tropic Heat 2, and other theoretical studies. A summary is presented in Section 8.

2.2 Background conditions

2.2.1 The data

During TIWE, R/V WECOMA occupied station at 0°N, 140°W for 21 days from 4 November to 25 November, 1991. Intensive measurements of microstructure were made almost continuously day and night. Our microstructure profiler Chameleon [Moum *et al.*, 1995] obtained measurements of conductivity, temperature, microstructure shear (from which turbulent kinetic energy dissipation rate ϵ was computed) and pressure from near the surface, down to about 200 m depth. Each individual microstructure profile took about 7–10 minutes to complete. A 150 KHz ship-board ADCP recorded current velocity, ensemble-averaged over 5 minutes [Lien *et al.*, 1994]. It used a 16-m pulse length and an 8 m bin width. The shallowest bin was centered at 20 m, and the deepest bin was near 500 m depth. The resulting ADCP velocities were smoothed volume averages of current velocity with 8 m vertical resolution.

Two towed thermistor chains (T-chains) provided continuous time series of temperature profiles to about 50 m depth. The chains were deployed on the starboard side, one aft, one forward, with a horizontal spacing of 43 m. There were a total of 11 thermistors on each chain with vertical spacing of 3 m. The sampling interval was 10 Hz. The temperature time series from the T-Chains were averaged

over 10 seconds. The two chains were out of operation for two hours every second day while the ship was repositioned.

On November 9, 1991, an especially energetic wave event was observed from both T-chains. Temperature time series from the thermistors at 35 m showed a remarkably well-defined wave structure that lasted for several hours (Figure 2.1a). High turbulent kinetic energy dissipation rate penetrated deeper after these waves appeared (Figure 2.1d). We thus choose the hourly averaged profiles of this 24-hour period for our stability analysis, with the intention of comparing the stability characteristics with observations.

2.2.2 Basic state for the linear stability analysis

In this subsection, we discuss the time-depth variations of several properties of the background flow that govern dynamic instability. These include zonal velocity $U(z)$, meridional velocity $V(z)$ (z is the vertical coordinate), the magnitude of the vertical shear $S = \sqrt{U_z^2 + V_z^2}$ (subscript z denotes differentiation), and Brunt-Väisälä frequency $N = \sqrt{-g\rho_z/\rho_0}$, where $\rho(z)$ is the mean density field, ρ_0 is the reference density, usually taken as the average value of the density over the water column.

Figures 2.2 and 2.3 illustrate the upper ocean conditions that prevailed on Nov. 9, 1991. Above 50 m, the zonal flow was dominated by the westward-flowing South Equatorial Current (SEC). We observed a well-developed EUC core between about 100 m and 140 m, with maximum eastward speed near 1 m s^{-1} (Figure 2.2a). The meridional velocity was much weaker, with maximum speed near 0.2 m s^{-1} , and was dominated by oscillatory motions (Figure 2.2b). Strong shear was observed both above and below the EUC core, and in a third layer near 180m depth (Figure

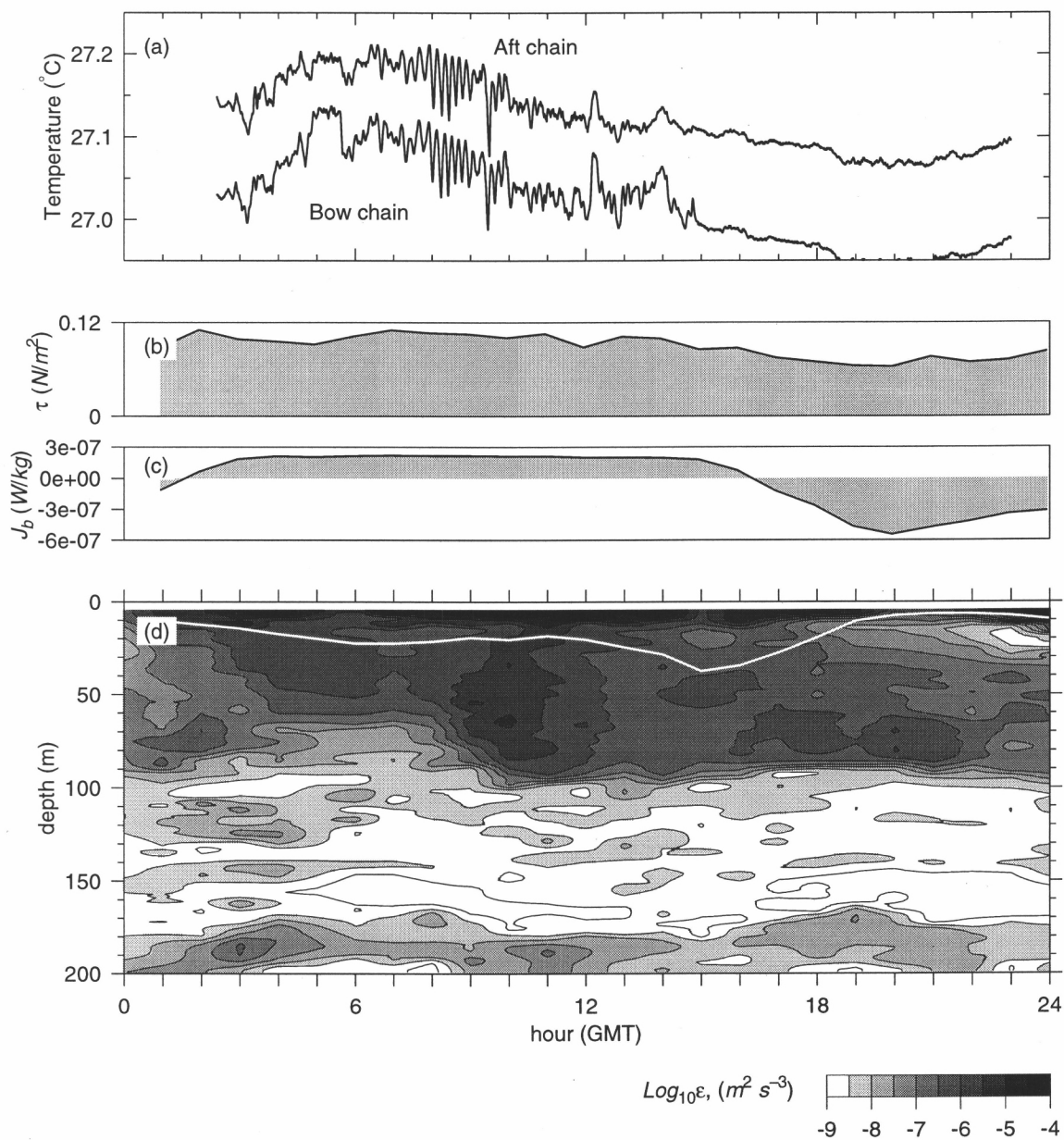


FIGURE 2.1. (a) Time series of temperature at 35 m from two thermistors deployed over the side of the ship, one at the bow and one aft. The data shown were obtained on day 313, 1991 at $0^\circ N$, $140^\circ W$ during TIWE. The two time series are offset by 0.1° . (b) Surface wind stress τ ($N m^{-2}$) (c) Surface buoyancy flux J_b ($W kg^{-1}$) (d) Logarithm of hourly averaged turbulent kinetic energy dissipation rate ϵ ($m^2 s^{-3}$) for the same time period. White line denotes the base of the surface mixed layer.

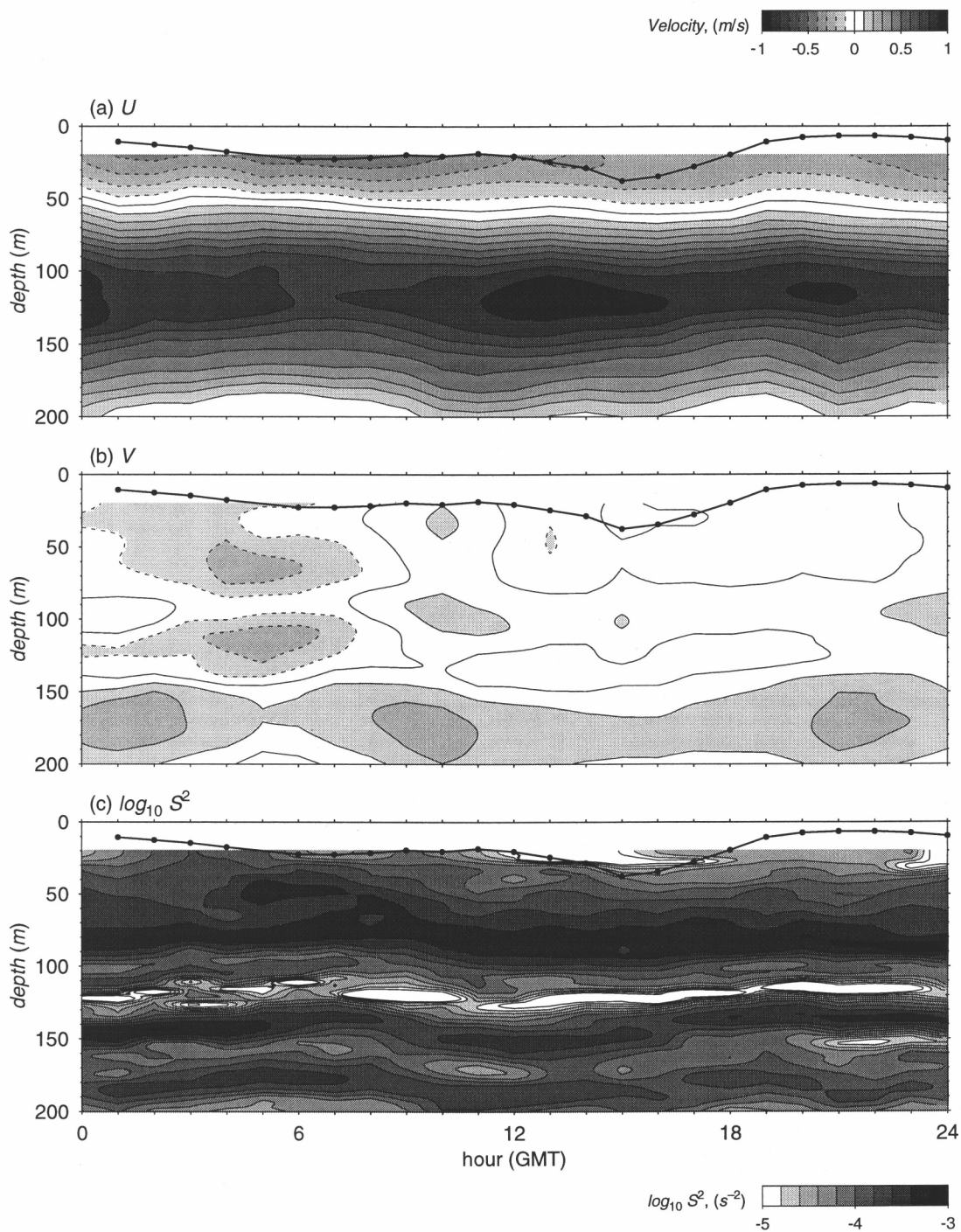


FIGURE 2.2. Hourly averaged (a) zonal, (b) meridional velocity, (c) logarithm of total shear squared $\log_{10} S^2$ on the same day as in Fig. 2.1. The black line with bullets represents the base of the surface mixed layer.

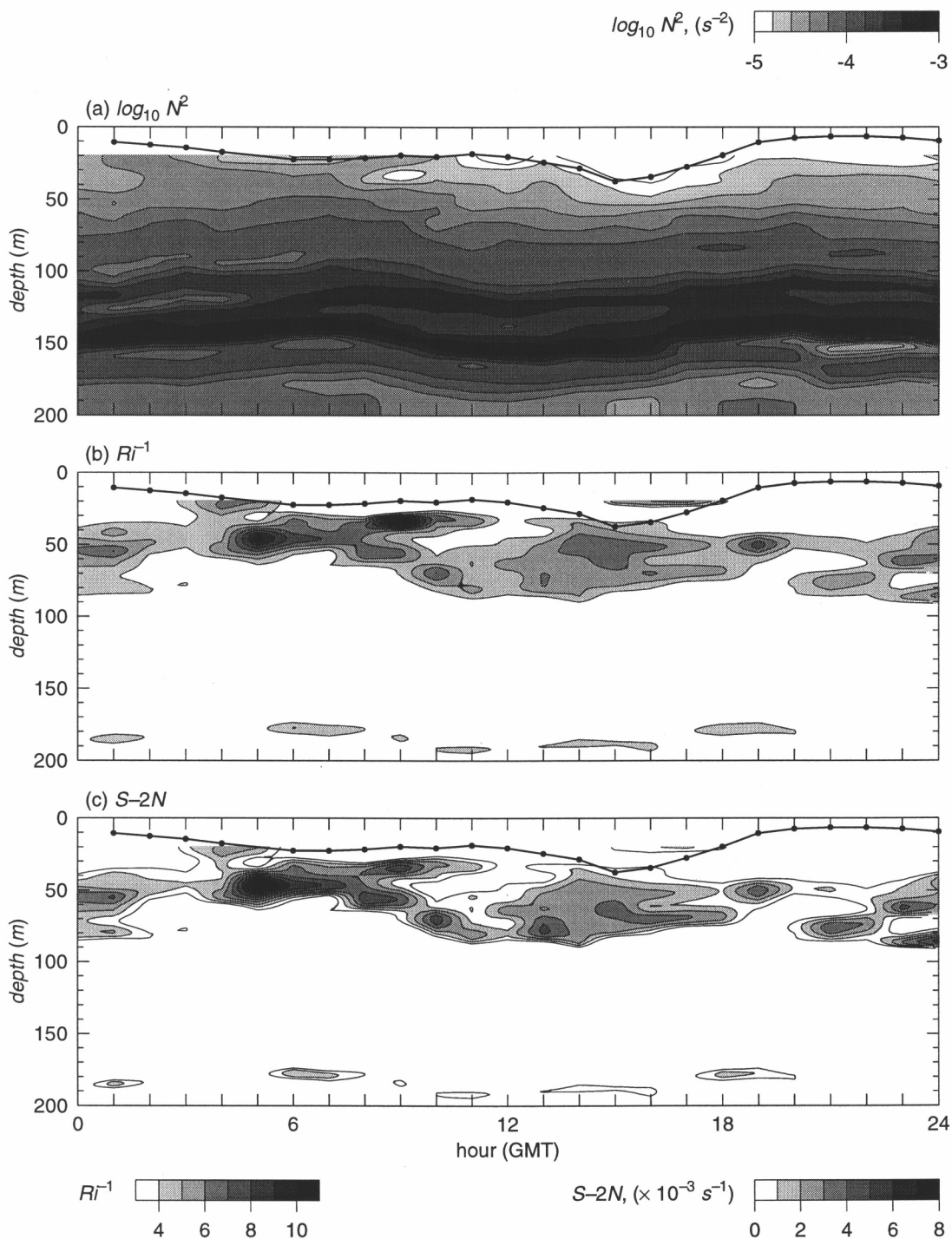


FIGURE 2.3. Hourly averaged (a) logarithm of buoyancy frequency squared $\log_{10} N^2$ (b) inverse gradient Richardson number Ri^{-1} and (c) reduced shear $S-2N$ on the same day as in Fig. 2.1. The black line with bullets denotes the base of the surface mixed layer.

2.2c). Also, note the brief shear episode that began at hour 5 near 50m depth. This episode led to intense shear instability, as we will show later. The strongest density stratification was found in the core of the EUC (Figure 2.3a). The weakest stratification occurred near the surface at night in association with the diurnal cycle of surface forcing.

It is common practice to use the gradient Richardson number ($Ri = N^2/S^2$) to diagnose shear instability, i.e. instability is expected if Ri is smaller than $1/4$, based on the well-known theorem of *Miles* [1961]. We argue here that this approach is naive. The Richardson number only indicates the *efficiency* with which an instability may extract kinetic energy from the mean flow; one also needs a measure of kinetic energy available for extraction. Consider, for example, a flow in which the $N = 0$, and S is nonzero but small. In this case, $Ri = 0$ and the flow may well be unstable, but growth rates of unstable modes may nevertheless be zero for all practical purposes. A better diagnostic of shear instability would take account of the absolute magnitude of the shear, as well as its magnitude relative to N . Such a diagnostic has been suggested by *Kunze et al.* [1990], who re-analyzed the theoretical results of *Hazel* [1972] to show that, over a substantial range of Ri , growth rates of Kelvin-Helmholtz modes growing on a hyperbolic-tangent shear layer are nearly proportional to $S - 2N$. *Sun et al.* [1997] show that this proportionality is also approximately valid for the much more complex flow geometries found in the ocean. We refer to the quantity $S - 2N$ as the *reduced shear*, and make frequent use of it in interpreting our results.

Subcritical values of Ri (i.e. $Ri < 1/4$) were observed at approximately 30-90 m depth throughout the 24-hour period of study (Figure 2.3b), and intermittently at the deep shear layer located near 180m depth. These coincided (by definition) with positive values of reduced shear (Figure 2.3c). The smallest values

of Ri occurred at hour 9 near 35 m depth. However, values of the reduced shear were not especially large at that point. The largest value of reduced shear occurred at hour 5 near 50 m depth. We will see that this is the location where the water column was most unstable.

In subsequent sections, we will use profiles of the hourly-averaged data shown in figures 2 and 3 as input to the Taylor–Goldstein equation, and compute the stability characteristics of the water column throughout the 24-hour period of study.

2.3 The eigenvalue problem

We consider the 3-dimensional Taylor–Goldstein equation [e.g., *Boyd et al.*, 1993], where the background flow has both zonal and meridional velocity components. The details of derivation of the Taylor–Goldstein equation are presented in Appendix A. We assume a normal mode solution,

$$[u', v', w', p', \rho'] = \text{Re}\{[\hat{u}(z), \hat{v}(z), \hat{w}(z), \hat{p}(z), \hat{\rho}(z)]e^{i(kx+ly-\omega t)}\} \quad (2.1)$$

where primed variables represent perturbations from the background state as defined in section 2. $\mathbf{K} = (k, l)$ is the horizontal wavenumber vector, k and l are zonal and meridional wavenumbers, respectively. $\kappa = \sqrt{k^2 + l^2}$ is the amplitude of horizontal wavenumber vector. $\omega = \omega_r + i\omega_i$ is the complex frequency. ω_r is the fixed frequency of the normal mode in a motionless frame, ω_i is the growth (or decay) rate.

For an inviscid, incompressible, stratified, shear flow, making the Boussinesq approximation, the 3-dimensional stability equation is

$$\hat{w}_{zz} + \left\{ \frac{N^2}{(\bar{U} - c)^2} - \frac{\bar{U}_{zz}}{\bar{U} - c} - \kappa^2 \right\} \hat{w} = 0. \quad (2.2)$$

where $\mathbf{U}(z) = (U(z), V(z), 0)$, $U(z)$ and $V(z)$ represent velocity components in the zonal and meridional directions, respectively. \bar{U} is the component of the mean flow

parallel to the horizontal wavenumber, $\tilde{U} = \mathbf{U} \cdot \mathbf{K}/\kappa = U \cos \theta + V \sin \theta$, where $\theta = \tan^{-1}(l/k)$ is the wavenumber direction. N is the local buoyancy frequency, defined by $N^2(z) = -g\bar{\rho}_z/\rho_0$. $c = c_r + ic_i$ is the complex phase velocity, $c = \omega/\kappa$. $\omega_i = \kappa c_i$ represents the growth (decay) rate of an unstable mode if $c_i > 0$ (< 0). c_r is the phase speed.

At the ocean surface, we require the vertical velocity of the perturbation to be zero. A radiation boundary condition is imposed at the lower boundary, so that waves generated at the shear layer can propagate downward into the thermocline (Appendix B). The Taylor–Goldstein equation and the boundary conditions constitute an eigenvalue problem which implicitly defines the dispersion relation $c = c(\mathbf{K})$.

2.4 Numerical method

We apply a shooting method [Press *et al.*, 1992] to solve the eigenvalue problem, similar to that used by Hazel [1972]. We modified it to account for the complexity of the background profiles used here. This shooting method integrates (2.2) from one boundary to the other, using a fifth-order adaptive step-size Runge–Kutta scheme. For given values of κ and θ , as well as an initial guess for c , it tries to match the boundary condition at the other boundary by adjusting the value of c . It thus defines a matching function with c being the independent variable. A globally convergent Newton’s method is utilized to locate the complex eigenvalue c .

2.4.1 Data processing

To incorporate the measured current and density profiles into the numerical scheme, we first need to define a “basic state”, upon which small disturbances

might grow. *Lien et al.* [1996] showed that wave signals observed from a moored thermistor chain had frequencies greater than 1 cph at our location and about the same time. We thus choose hourly averaged data as background profiles for the stability analysis. (*Smyth and Peltier* [1994] have shown that, on a time-varying background flow, the growth of unstable modes over a finite interval Δt can be predicted via stability analysis of the background flow averaged over Δt . The results become exact for growth rates $\gg 1/\Delta t$.) To match the inherent filtering of current velocity by shipboard ADCP with a 16-m pulse length [*Lien et al.*, 1994], hourly averaged density profiles are smoothed by a 16-m triangular filter.

To obtain a continuous distribution of velocity and density as functions of depth, we employ (natural) cubic splines to interpolate between the discrete values provided by the data. As we have mentioned in Section 2, the velocity data by the shipboard ADCP are vertical profiles recorded at intervals of 8 m. From the surface to 20 m depth, the velocity is linearly extrapolated. The velocity thus obtained agrees well with measurements at depths of 3 m and 10 m from a nearby NOAA Pacific Marine Environmental Laboratory (PMEL) mooring. The filtered density profiles are sampled at 4 m intervals, then interpolated using cubic splines. (This slight mismatch in processing of currents and density is necessitated due to spurious convective overturns resulted from cubic spline interpolation for density profiles in 8-m vertical intervals.)

The resulting second order derivatives of velocity U_{zz} and V_{zz} are piecewise linear functions of depth over every 8 m interval. To properly manage the discontinuities in the derivatives of U_{zz} and V_{zz} , the integration of (2.2) is done in steps from one data point to the next, so that the evaluation of the derivatives of U_{zz} and V_{zz} across data points are avoided.

2.4.2 Range of wavenumbers

Our objective is to obtain the eigenvalue c for given wavenumbers. For each choice of κ and θ , we solve the equivalent two-dimensional problem with the profiles of mean horizontal velocity vector projected on a vertical plane in the direction θ , i.e. $\tilde{U}(z)$. We first need to decide the range of directions to be investigated. As we have shown in Appendix B, the Miles–Howard theorem is valid for a radiation lower boundary condition. As a result, if Ri is greater than 0.25 at every depth, the flow is stable. If the projected mean flow in the direction θ has $\tilde{R}i$ ($\tilde{R}i = N^2/\tilde{U}_z^2$) greater than 0.25 at every depth, the flow is stable to small perturbations whose wavenumber vector is in that direction. This helps us to eliminate those stable directions from computations of the eigenvalue. By symmetry, only half the wavenumber domain needs to be considered; we choose the range of θ to be $[-90^\circ, 90^\circ]$.

The range of the magnitude of wavenumbers κ is not as clearly identified as that of θ . For a hyperbolic tangent profile, the wavelength of the unstable waves is proportional to the shear-layer depth, which is defined as the depth over which the current shear is large. The wavelength of the fastest growing instability ranges from 4 to 8 times the shear-layer depth [e.g., *Drazin*, 1958; *Miles and Howard*, 1964; *Davis and Peltier*, 1976]. For the complicated profiles considered in this paper, there is no such well-defined “shear layer”. We restrict the stability analysis to values of the wavenumber κ ranging from 5×10^{-4} rad m $^{-1}$ to 10^{-1} rad m $^{-1}$, at intervals of 5×10^{-4} rad m $^{-1}$. The corresponding wavelengths range from 63 m to 12570 m. This includes the range of wavelengths found by *Moum et al.* [1992] from towed thermistor-chain data and by *McPhaden and Peters* [1992], also by *Levine and Moum* [1997] from data obtained in this experiment.

2.4.3 Initial guesses for the eigenvalue

The shooting method requires an initial guess for the complex eigenvalue c . We look for all the eigenvalues with a positive c_i , which represents growth with time. The bounds on the complex phase speed c depend on the range of velocity, and are given by Howard's semi-circle theorem (Appendix B). For the non-parallel background flows considered here, the range of velocity is in turn a function of θ . To find all possible unstable modes, we provide a set of initial guesses (typically 10) chosen to lie inside Howard's semi-circle.

2.5 Detailed study of unstable modes from a single hour

We first investigate the unstable modes for one hour in detail, then we summarize the general properties of unstable modes for every hour of day 313. As we will see later, hour 5 (local time: 20:00) has the highest growth rate. Due to incomplete data at hour 5, we choose hour 6 (the hour with the second largest growth rate) as a focus for detailed study in the remainder of this section.

2.5.1 Mean profiles during hour 6

During hour 6, the zonal flow above 50 m was dominated by the westward-flowing South Equatorial Current (Figure 2.4a). The core of the eastward-flowing EUC was located between about 100 and 120 m, with a maximum speed near 0.8 m s^{-1} . Meridional flow was southward above 150 m and exhibited oscillatory structure in the vertical (Figure 2.4b). The largest shear occurred near 50 m and 80 m. N^2 was largest around 140 m (Figure 2.4c). Though the total shear was dominated by its zonal component, meridional shear contributed to the shear max-

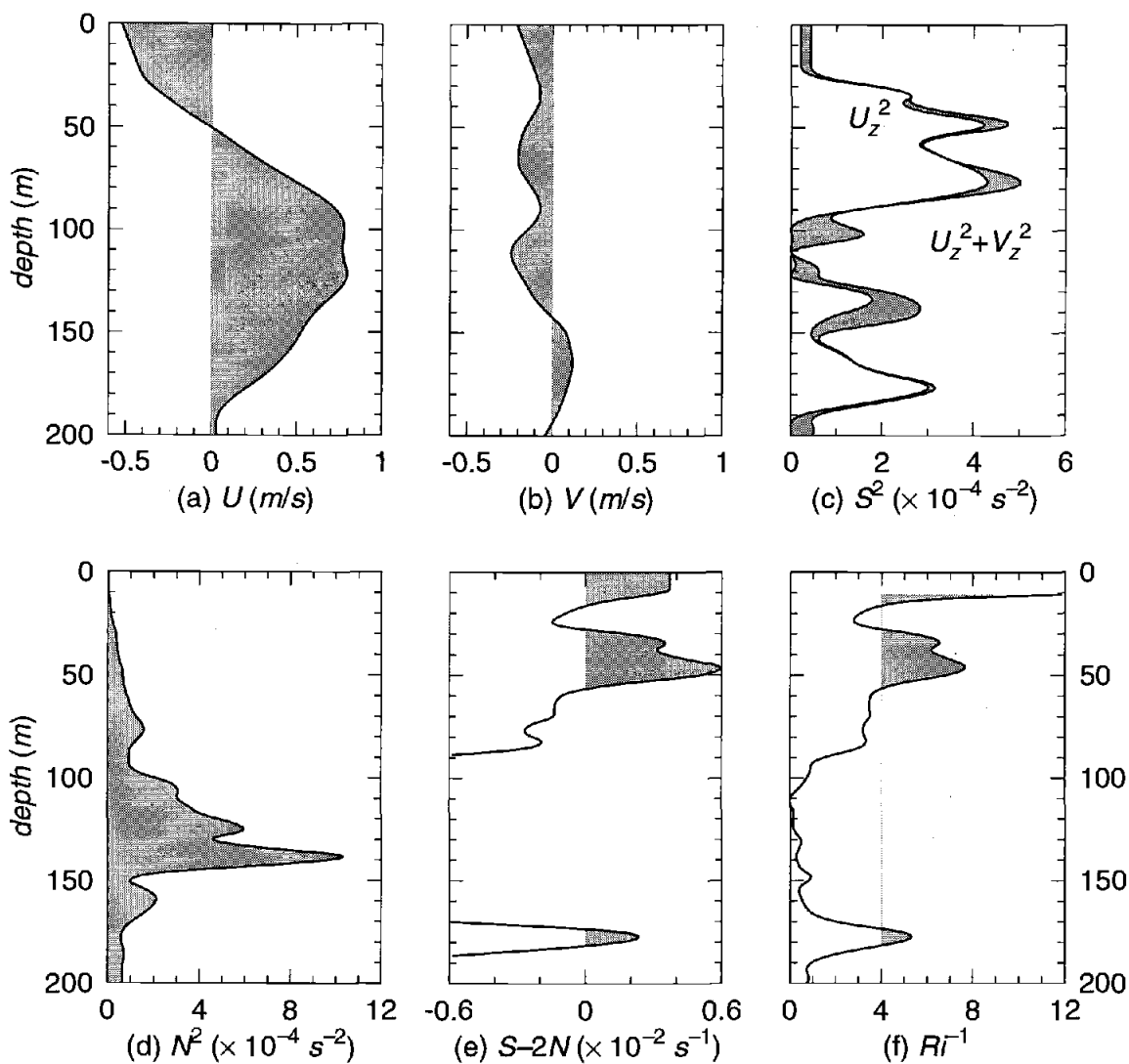


FIGURE 2.4. Background profiles of hour 6 on year day 313. (a) zonal velocity U , (b) meridional velocity V , (c) total shear squared $U_z^2 + V_z^2$ and zonal shear squared U_z^2 . The meridional shear squared is represented by the shaded region. (d) buoyancy frequency squared N^2 , (e) $S - 2N$ (f) Ri^{-1} .

ima at these two depths. The high shear and relatively weak stratification resulted in a maximum of reduced shear $S - 2N$ near 50 m (Figure 2.4d and 2.4e). The stratification near 80 m was strong enough to cause Ri to be greater than the critical value $1/4$ there. Three regions had positive reduced shear (or $Ri < 1/4$): the surface mixed layer (from the surface to about 16 m), deep-cycle region (28–57 m) and a thin layer below both the EUC core and the main pycnocline (173–181 m) (Figure 2.4f).

In the surface mixed layer, Ri dropped to nearly zero, suggesting strong instability. On the other hand, the reduced shear is not especially large, and instability may be dampened by boundary effects. In fact, we will see that the deep cycle layer and the deep shear layer at 180 m are the main sites of instability.

2.5.2 The dispersion relation

Typically, the dispersion relation $\omega = \omega(k, l)$ is not single-valued. Instead, it exhibits several overlapping surfaces upon which ω varies continuously. On each surface, the growth rate, $\omega_i = \kappa c_i$, varies significantly, while the phase speed $c_r = \omega_r / \kappa$ is relatively constant. What this means physically is that each surface represents a continuum of unstable modes whose critical levels are close to a given depth (usually a depth at which reduced shear is large, or Ri is small). We refer to each of these continua as a “family” of unstable modes. Each family has a “fastest growing mode” (FGM), the mode whose wave-vector (k, l) is such that the transfer of energy from the mean flow is optimized and thus the growth rate is a maximum. This is the mode that is expected to dominate in the long-time limit. In reality, disturbances grow over finite times, so that modes other than the “most unstable mode”, the mode with the largest growth rate among all unstable modes, will also

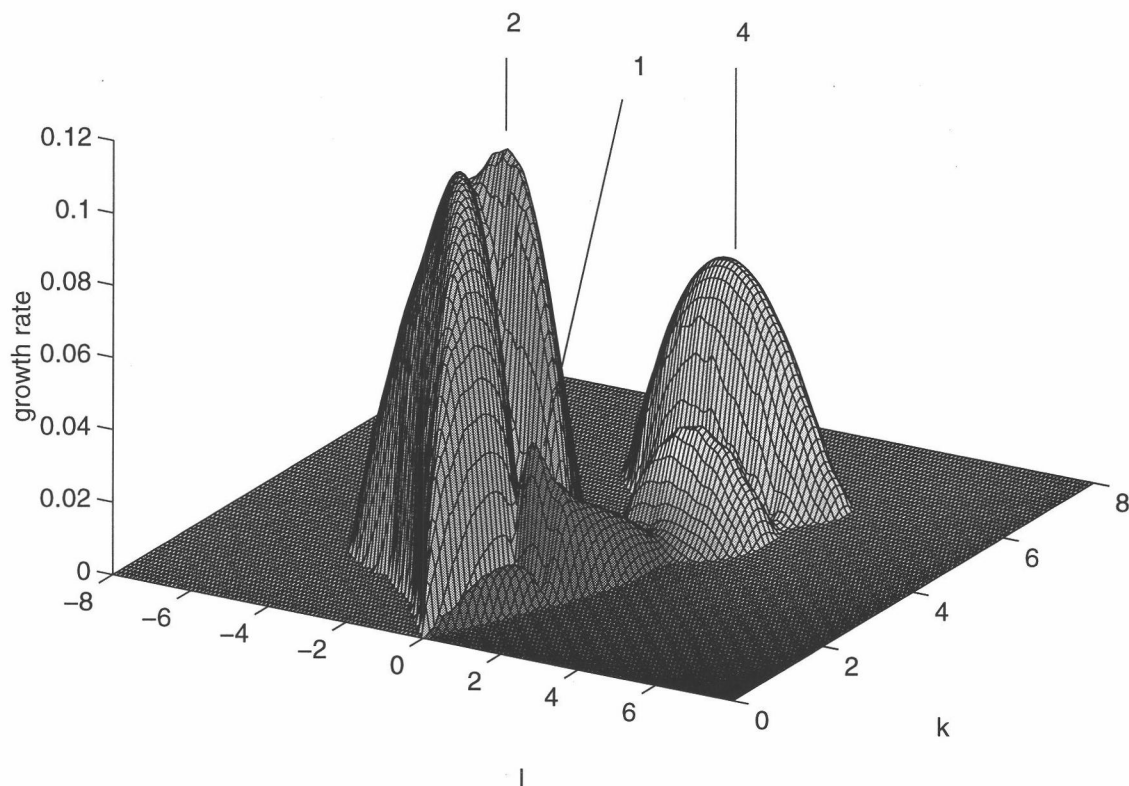


FIGURE 2.5. Growth rate and critical level versus zonal and meridional wavenumbers k (10^{-2} rad/m) and l (10^{-2} rad/m). The height represents the growth rate (10^{-2} s $^{-1}$). Shading represents the critical level of each mode. The numbers 1, 2 and 4 refer to modes 1, 2 and 4. Each mode is characterized by a different phase speed, according to the depth of its critical level.

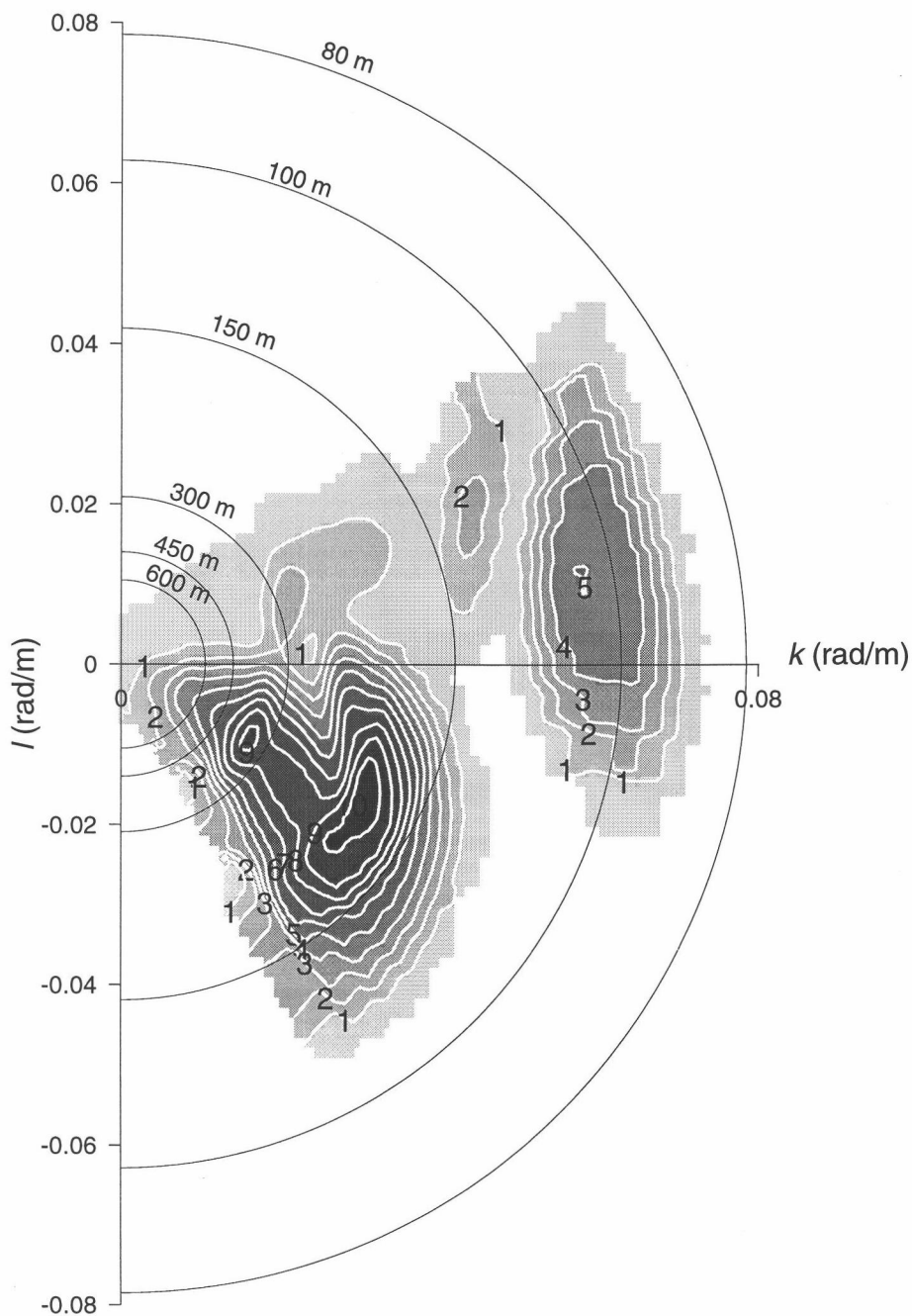


FIGURE 2.6. Contour plots of growth rate and critical level versus zonal and meridional wavenumbers, k and l , for the background conditions of hour 6 on day 313. Half circles represent constant wavelengths.

have significant amplitude. As a result, each mode family is expected to generate a wave packet. The horizontal scale of the wave packet is inversely proportional to the width of the growth rate maximum on the (k, l) plane, and grows with time, so that the idealization of a monochromatic wavetrain is realized in the limit $t \rightarrow \infty$.

Three families of unstable modes can be identified for hour 6 (Figure 2.5). Their growth rates and phase speeds were very different. We denote the mode family with westward propagation direction as mode 1, the mode family with almost zero phase speed as mode 2, and the mode family with eastward propagation direction as mode 4. (The reason for this denumeration will be clear in Section 6.) Mode 1 has the smallest growth rate $4 \times 10^{-4} \text{ s}^{-1}$, and propagates to WSW with a speed of 0.3 m s^{-1} . Mode 2 has the largest growth rate, $2.1 \times 10^{-3} \text{ s}^{-1}$, and phase speed very close to zero. It has a bimodal structure, with comparable growth rates for the two peaks. Mode 4 propagates to ENE with a speed of 0.2 m s^{-1} . Its growth rate was $6.4 \times 10^{-4} \text{ s}^{-1}$. The wavelengths of these unstable modes range from about 80 m to 450 m (Figure 2.6). The characteristics of these three unstable modes of the mean flow observed during hour 6 are summarized in Table 2.1.

Measured velocity profiles from shipboard ADCP are not ideal candidates for stability analysis, since they underestimate the shear due to vertical averaging [e.g., *Lien et al.*, 1994; *Pedlosky*, 1987, §7.1]. In addition, the 1-hour averaging process that we use to remove waves from the background flow tends to smooth vertical gradients. The result of this smoothing is to raise Ri (or lower the reduced shear), and thus to reduce the growth rates. In the profiles we study, instability was sufficiently strong that stabilization by smoothing of background profiles was not a dominant factor. Nevertheless, our estimates of growth rates are likely to be on the low side.

Table 2.1. Parameters of the fastest growing modes of three mode families of hour 6 during day 313

Mode	λ (m)	θ ($^\circ$)	ω_i (s^{-1})	T_e (min)	c_r ($m\ s^{-1}$)	ω_r (cph)	z_c (m)	z_R (m)
1	300	195	4.0×10^{-4}	41.7	0.30	3.6	35	34
2	188	335	1.1×10^{-3}	15.3	0.00	0.0	47	46
4	106	10	6.4×10^{-4}	26.0	0.20	6.8	176	177

λ is the wavelength of the unstable mode. θ is the direction of its propagation. ω_i is the growth rate. T_e is the corresponding e-folding time. c_r is the real part of the complex phase speed. ω_r is the frequency of unstable mode relative to the ground. z_c is the depth of critical level. z_R is the depth of local *Ri* minimum nearest to the critical level of each unstable mode.

2.5.3 Vertical structure of unstable modes

Because (2.2) and its boundary conditions are linear and homogeneous, the absolute value of the amplitudes of the eigenfunctions cannot be determined. We normalize the solutions by scaling the maximum amplitude of vertical velocity to unity. The vertical velocity of modes 1 and 2 has significant amplitude throughout the 200 m domain (Figure 2.7a). The phase of \hat{w} is shown as the dashed line. The amplitude of \hat{w} of mode 2 goes to zero near the lower boundary, while the amplitudes of \hat{w} of modes 1 and 4 remain substantial (Figure 2.7b, 2.7c). This suggests a significant radiation of energy through the lower boundary. Interestingly, the largest amplitude of vertical velocity of mode 1 occurs at the EUC core at about 100 to 120 m. The vertical velocity of mode 4 only has significant amplitude below about 70 m, but is large at the lower boundary.

The critical level of a normal mode perturbation is the depth at which the velocity of background flow matches the phase velocity. Each unstable mode is clearly associated with a distinct critical level. Mode 1 has the shallowest critical level at 35 m depth. The critical level of mode 2 corresponds to the shear maximum at 47 m. Mode 4 has a deep critical level near 176 m. Profiles of vertical velocity indicate a typical Kelvin–Helmholtz structure: a minimum at the critical level and maxima at either side. The phase of \hat{w} changes across the critical level, but is relatively constant above and below the critical level.

To better understand the physics of unstable modes, we examine the depth-dependent kinetic energy equation for small 3-D disturbances in an inviscid stratified shear flow

$$\frac{1}{2}(\overline{u'^2} + \overline{v'^2} + \overline{w'^2})_t = (-\overline{u'w'}U_z - \overline{v'w'}V_z) - g\overline{\rho'w'} - \overline{(p'w')}_z \quad (2.3)$$

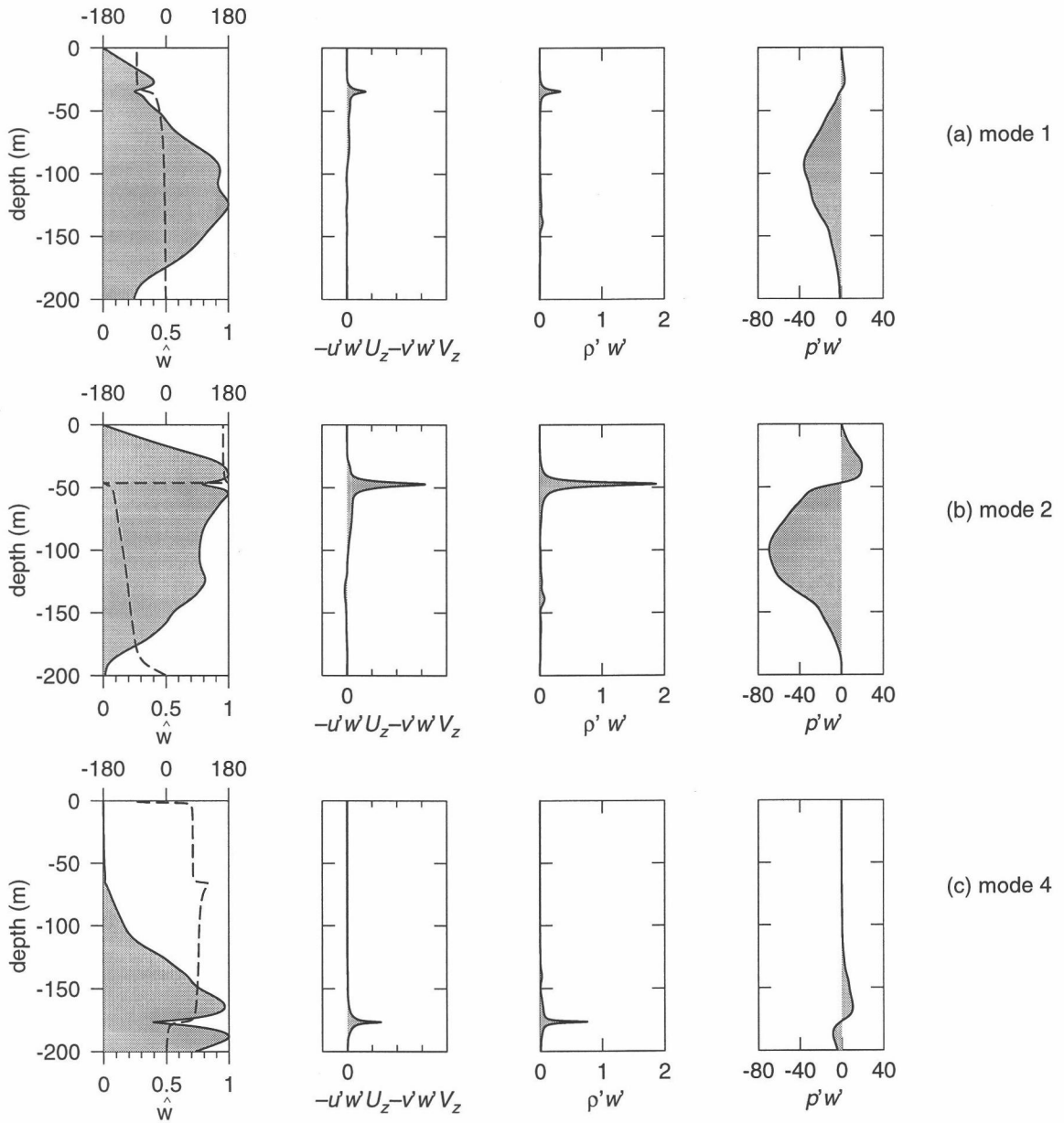


FIGURE 2.7. Eigenfunctions of the dominant mode of each of the three families of unstable modes present at hour 6. Column 1: vertical velocity \hat{w} (solid line) and its phase (dashed line) for the three unstable modes of hour 6 shown in Figures 2.5, 2.6. Column 2: shear production of kinetic energy $-\overline{u'w'U_z} - \overline{v'w'V_z}$. Column 3: buoyancy flux $\overline{\rho'w'}$. Column 4: vertical flux of perturbation kinetic energy $\overline{p'w'}$.

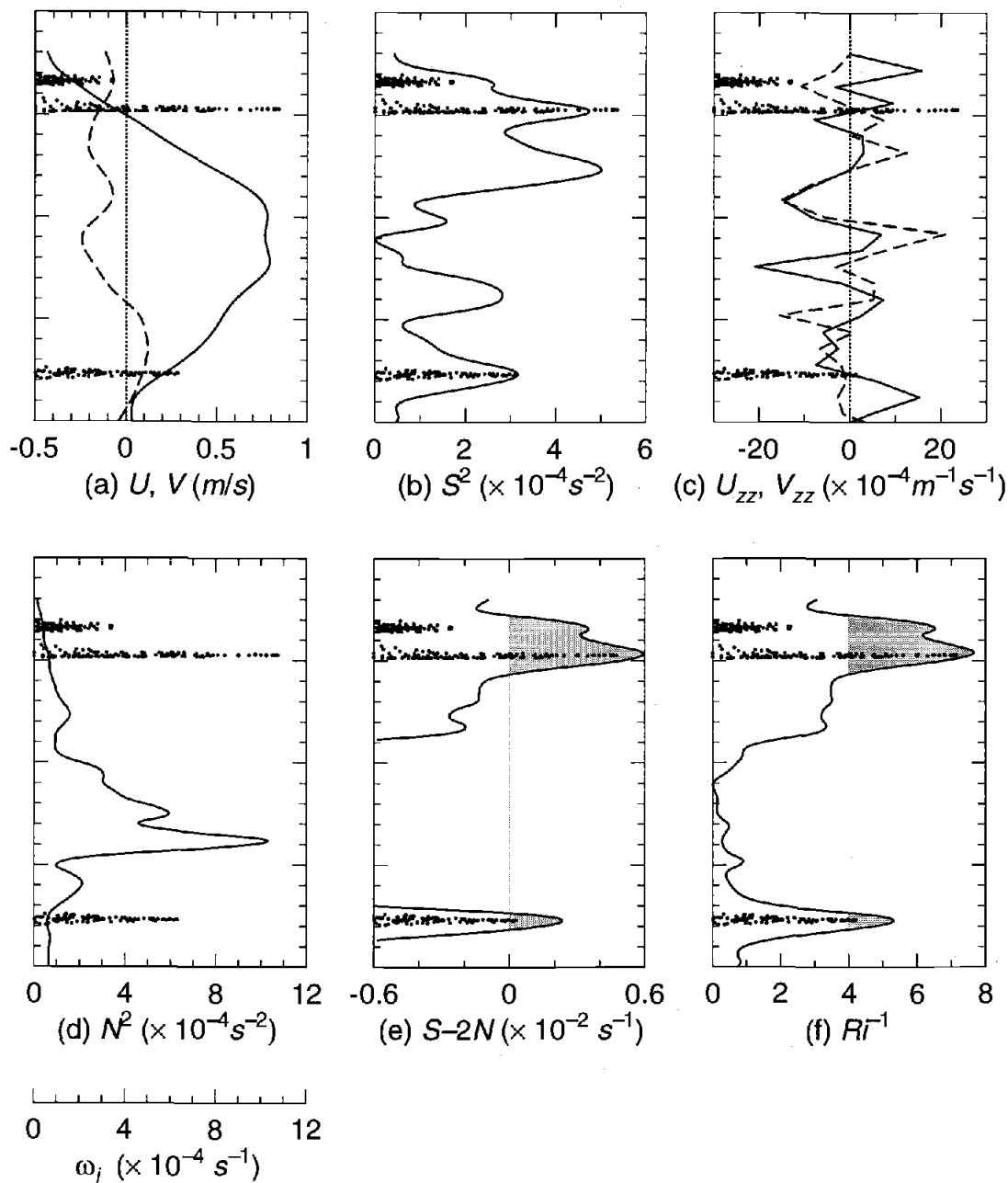


FIGURE 2.8. Growth rates ω_i ($\times 10^{-4} s^{-1}$) versus critical levels of all unstable modes superimposed on profiles of background quantities. (a) U (solid line) and V (dashed line), (b) S^2 , (c) U_{zz} (solid line) and V_{zz} (dashed line), (d) N^2 , (e) $S-2N$, (f) Ri^{-1} . The mode family with critical levels centered around 35 m corresponds to mode 1 in Fig. 2.5. The mode family with critical levels centered around 50 m corresponds to mode 2 in Fig. 2.5. The mode family with critical levels centered around 175 m corresponds to mode 4 in Fig. 2.5.

where the overbar denotes average over one horizontal wavelength. The terms on the right hand side represent shear production, work done by gravity, and the convergence of the vertical energy flux, respectively. Both shear production and gravitational work are strongly concentrated at the critical level (Figure 2.7, columns 2 and 3). The vertical flux of perturbation kinetic energy $\overline{p'w'}$ is positive above the critical level and negative below it, i.e., perturbation kinetic energy is transported outward from the critical layer to the other regions of the flow. For modes 1 and 2, the kinetic energy is extracted from the upper thermocline and redistributed throughout the whole domain. For mode 4, the energy flux $\overline{p'w'}$ has significant magnitude at the lower boundary. This indicates that this mode is capable of transporting energy vertically into deeper regions. The buoyancy flux due to the disturbance $\overline{\rho'w'}$ is positive throughout the domain. This is anticipated because, in stable stratification, a part of the kinetic energy extracted from the background shear is used to increase the potential energy of the flow.

We now seek to identify the particular characteristics of the background profiles at hour 6 (cf. Figure 2.4) that govern the growth rates and phase velocities of the unstable modes. To do this, we plot the growth rates of all of the unstable modes that our shooting code has identified at hour 6 (Figure 2.8). The vertical location of the point corresponded to the critical level of a given mode; the horizontal coordinate is its growth rate. The modes are superimposed on profiles of various background quantities. Critical levels of unstable modes tend to cluster in thin layers surrounding the maxima of the reduced shear (which tend to coincide with minima of Ri). It is clear from these results that the reduced shear and the Richardson number are the best indicators of instability.

2.6 Variability of shear instability over a 24-hour period

We now examine the stability characteristics of the upper ocean during the entire 24-hour period of study (Figure 2.9). Since there were no microstructure measurements during hour 5, we interpolated the background density profile from the two neighboring hours (velocity data were available from the ADCP). To be sure that the resulting smoothing of the density profile did not introduce artificial effects in the stability analysis, we repeated the calculations using the density profile of hour 4 alone, then again using the hour 6 profile. The fastest growing modes calculated using the density profiles of hours 4 and 6 differ by only 2–4% of that from the calculations using interpolated density profile. This assures us that hour-to-hour changes in stability properties are governed mostly by changes in shear, so that approximation of the missing density profile does not give misleading results.

We organize our results by defining four regimes of instability, based on the zonal current structure (cf. Figure 2.9c).

- 1) Nearest the surface, the westward-flowing SEC was unstable throughout hours 6–11, then became stable as local Ri increased above $1/4$. We refer to this instability of the near-surface region (i.e. to unstable modes having critical levels in this layer) as “mode 1”. Mode 1, by definition, has zonal phase velocity directed to the west (Figure 2.10b). In the next section, we will show that this mode explains concurrent observations of wavelike disturbances.
- 2) Our second regime of instability lies on the boundary between the SEC and the eastward-flowing EUC, where the zonal velocity is near zero. We refer to instabilities with critical levels in this region as “mode 2”; more specifically, the critical level of mode 2 lies between the $U = -10 \text{ cm s}^{-1}$ and $U = 10 \text{ cm s}^{-1}$ isotachs. This regime was unstable continuously from hour 5 to hour 9,

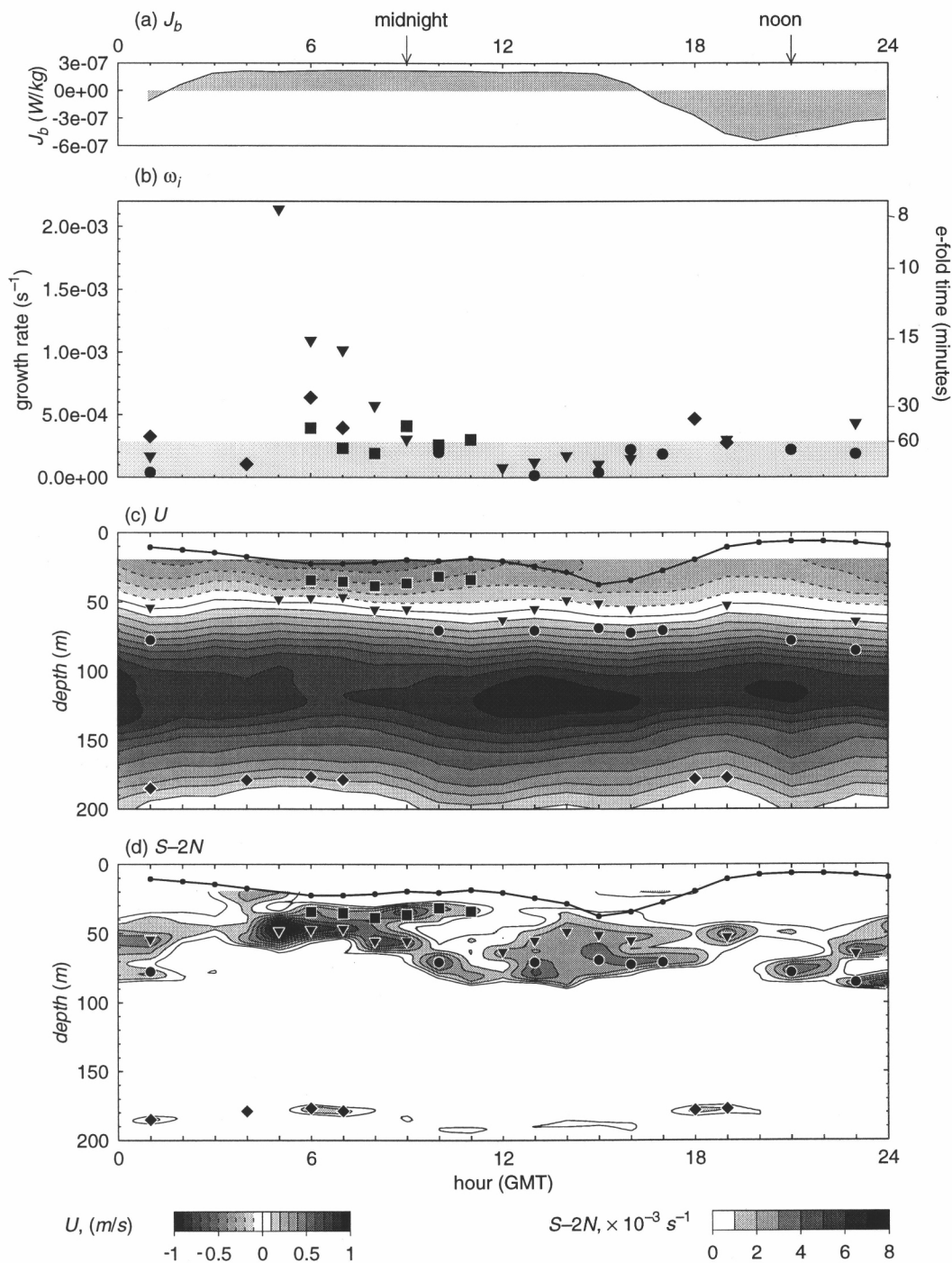


FIGURE 2.9. (a) Hourly averaged buoyancy flux J_b on day 313. (b) Growth rate of the unstable modes of each hour. The boxes, triangles, bullets and diamonds represent the growth rates of mode 1, 2, 3, and 4, respectively. (c) Image and contours of the zonal velocity. (d) Reduced shear $S - 2N$. The boxes, triangles, bullets and diamonds in (c) and (d) indicate the location of critical level of each mode.

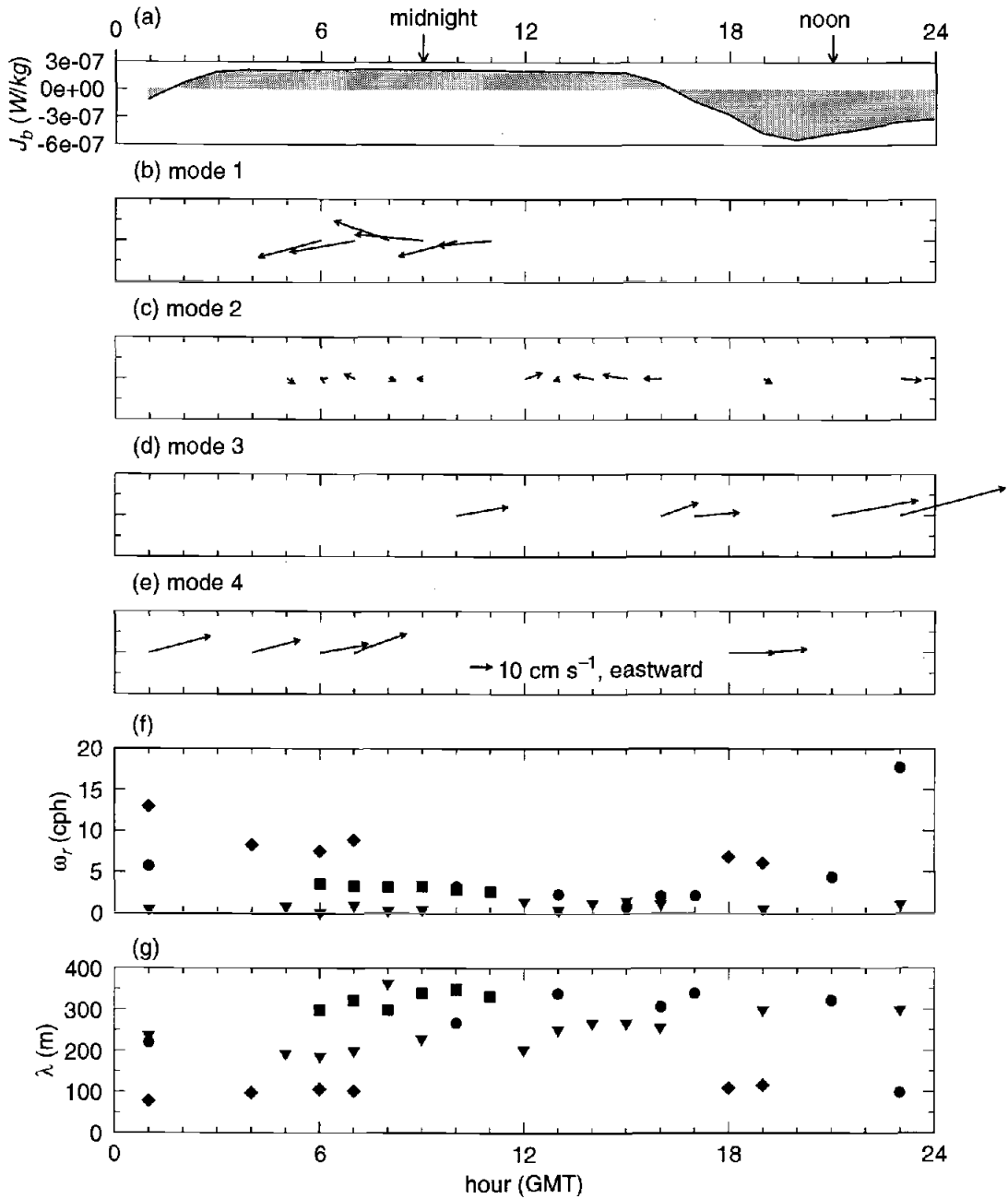


FIGURE 2.10. (a) Same as Fig. 2.9a. The phase velocities of mode 1, 2, 3 and 4 are shown in (b), (c), (d) and (e), respectively. Each arrow corresponds to an unstable mode. The direction and length of the arrow represent the direction of propagation (right=east, up=north) and magnitude of the phase velocity, respectively. A 10 cm s^{-1} scale is shown in (e). (f) The frequency of unstable modes seen by a stationary observer. (g) The wavelengths of unstable modes. The boxes, triangles, bullets and diamonds in (f) and (g) have the same meaning as in Figure 2.9.

then became unstable again after hour 12 (Figure 2.10c). The most energetic instabilities found in these calculations fall into the mode 2 category. The largest growth rate was obtained from background profile at hour 5, $2.1 \times 10^{-3} \text{ s}^{-1}$ (corresponding to an e-folding time less than 8 minutes). There were also strong instabilities in hours 6 and 7, with growth rates about $1.1 \times 10^{-3} \text{ s}^{-1}$ (corresponding to an e-folding time about 15 minutes). These episodes of intense instability occurred during the evening (hours 5, 6 and 7 correspond to local time 20:00, 21:00 and 22:00).

- 3) Our third class of modes had critical levels located on the upper flank of the EUC, and thus had eastward phase velocity (Figure 2.10d). This mode was unstable only intermittently, and exhibited very small growth rates during those times.
- 4) Our final class of instabilities, mode 4, was focussed in the thin shear layer at the bottom of the EUC, near 180 m depth. Like mode 3, this mode was weak and only intermittently unstable (Figure 2.10e).

2.7 Comparison with related studies

2.7.1 Concurrent observations of internal waves

An especially energetic wave event was recorded by both our thermistor chains during hours 7, 8 and 9 (Figure 2.1). *Levine and Moum [1997]* studied this wave packet in detail and estimated its frequency to be about 5 cph in the reference frame of the moving ship. A wave packet was simultaneously observed by a nearby mooring (*Lien et al. [1996]*). The estimated frequency from the mooring was 2–3 cph. Assuming the waves we observed were instability waves triggered by

random perturbations, we compare the frequencies of our unstable modes as seen by a stationary observer, and as seen from the ship's reference frame (Table 2.1), with the observations.

Mode 1 at hour 9 has frequency 3.3 cph in the reference frame of the earth, which becomes 4.2 cph in the reference frame of the moving ship. These frequencies compare rather well with the observations. However, T-chain records show similar wavelike activity during the previous hour. The shallow mode at hour 8 had frequency 3.2 cph in the earth frame, but in the ship's frame this becomes 2.4 cph, a poor fit to the observation. During hours 6 and 7, however, the calculated frequencies of mode 1 agree well with the observations. Because these instabilities grow with e-folding times on the order of an hour, it is plausible that there will be a time lag of a few hours between the onset of instability and the observation of large-amplitude waves. On the whole, there appears to be a significant correspondence between mode 1 and the wavelike oscillations observed at the same time.

The wavelength of mode 1 is about 300 m. *Levine and Moum* [1997]'s estimate of the wavelength is around 400 m. *Lien et al.* [1996] estimated a wavelength of 200–350m from the mooring measurement, assuming a westward propagating speed of 0.3 m s^{-1} .

The observations could also have been associated with the mode 2 instability. The latter was focussed in a similar depth range to mode 1, and had larger growth rates. However, the frequencies do not compare as well with the observations. At hour 5, mode 2 had a very large growth rate, and its frequency in the ship's frame was 4.7 cph, very close to what was observed a few hours later in the T-chain signals. This correspondence suggests that the observed waves could have been a remnant of the mode 2 instability at hour 5. However, the frequency of that mode in the earth's frame was much smaller than that observed at the mooring. In subsequent

Table 2.2. Parameters of the shallowest unstable mode from hour 5 to hour 9 during day 313 for comparison with observations

Hour	Mode	κ (rad m ⁻¹)	θ (°)	c_r (m s ⁻¹)	ω_i (s ⁻¹)	ω_r (cph)	ω_{ship} (cph)
5	2	0.0325	325	0.042	2.1×10^{-3}	0.8	4.7
6	1	0.0210	195	0.296	4.0×10^{-4}	3.6	6.8
	2	0.0335	155	0.002	1.1×10^{-3}	0.0	2.2
7	1	0.0195	190	0.300	2.3×10^{-4}	3.4	5.9
	2	0.0315	155	0.054	1.0×10^{-3}	1.0	1.1
8	1	0.0210	160	0.267	1.9×10^{-4}	3.2	2.4
	2	0.0173	340	0.030	5.7×10^{-4}	0.3	1.0
9	1	0.0185	175	0.311	4.1×10^{-4}	3.3	4.2
	2	0.0275	185	0.027	3.1×10^{-4}	0.4	3.2

κ is the magnitude of the horizontal wavenumber of the unstable mode. θ is the direction of the unstable mode. c_r is the phase speed. ω_i is the growth rate. ω_r is the frequency of unstable modes relative to the ground. ω_{ship} is the frequency of the unstable modes that would be observed from a ship moving with velocity (0.13, 0.55) m s⁻¹, the velocity of the R/V Wecoma during this period.

hours, mode 2 exhibits frequencies in the reference frames of both motionless earth and moving ship that compare poorly with the observations. These results suggest that the observed waves are indeed remnants of the mode 1 instability. It could be that the relatively small growth rates assigned to mode 1 are inaccurate, possibly because near-surface shear was underestimated by the ADCP, as suggested by Mack & Hebert (1997).

2.7.2 Internal waves observed during Tropic Heat 2

We have shown that shear instability is capable of generating coherent vertical structure over large vertical extent, far beyond the zone of small Ri . This kind of vertical structure is consistent with the observations of wave events during Tropic Heat 2. *Hebert et al.* [1992] showed that the vertical scale of an energetic wave event observed during Tropic Heat2 was greater than 125 m, much larger than the vertical extent of the low Richardson number region.

The wavelengths of unstable modes from our results are consistent with the observations of similar events during Tropic Heat 2. The wavelength of the wave event studied by *Hebert et al.* [1992] was about 100 m. From four days of observations of high-frequency internal waves in the same experiment, *Moum et al.* [1992b] estimated that the scale of vertical coherence of this band of waves was about 120 m. They found that the spectrum of vertical isotherm displacements was dominated by a narrow wavenumber band of internal waves with wavelengths between about 150 to 250 m. *McPhaden and Peters* [1992] estimated that the zonal wavelength of high-frequency waves observed from a mooring was about 100–300 m. These estimated wavelengths are consistent with our results.

2.7.3 Theoretical studies

Skyllingstad and Denbo [1994] studied the generation and evolution of the internal waves, using a two-dimensional nonhydrostatic model. One of the simulations they performed applied the initial state from the measured velocity and density profiles reported in *Hebert et al.* [1991]. They found that shear instability in the mixed layer was responsible for the generation of internal gravity waves. The wavelength of instability wave was about 250 m, with phase speed about -0.03 m s^{-1} . These values of wavelength and phase speed are similar to those of mode 2 in our study. Our results show that shear instability could be generated in the stratified layer below the surface mixed layer. In addition, we find that the unstable modes can radiate downward beyond the lower boundary.

Two recent analyses have focused on shear instability in the EUC. Modeling the upper flank of the EUC as a hyperbolic tangent profile, *Sutherland* [1996] solved the stability problem and showed that shear instability may generate downward propagating internal gravity waves, with a wavelength of about 100 m, and phase speed 0.5 m s^{-1} eastward. *Mack and Hebert* [1997] solved the same problem using more complicated analytical functions to approximate the background conditions during Tropic Heat 2. Because the measured Ri did not fall below $1/4$, they enhanced zonal shear in the upper 40 m to force Ri to be smaller. They found that the e-folding growing time for the most unstable mode for some cases was less than 10 minutes. The wavelength ranged from about 100 to 300 m. In all cases, the phase speed was westward, in the range of -0.8 to -0.1 cm s^{-1} .

Our analyses are consistent with these two studies. Like *Mack and Hebert* [1997], we find that a strongly sheared westward current near the surface leads to westward propagating unstable modes with e-fold growing time as small as 8

minutes. The difference in our case is that the strong near-surface shears were not hypothetical, but rather were observed by the combination of shipboard ADCP and the PMEL mooring. Like *Sutherland* [1996], we have examined a situation in which subcritical Richardson numbers exist in the upper flank of the EUC, and we thus find eastward-propagating unstable modes that radiate energy from the upper EUC into the deep ocean. To extend the results of *Sutherland* [1996], we have employed realistic velocity and density profiles, both above and below the EUC core, so that the complex wave propagation characteristics of the lower EUC and upper thermocline are represented in detail.

2.8 Summary

During TIWE, we made simultaneous measurements of velocity and density profiles in the mixed layer and upper thermocline at 0° , 140°W . Here, we have solved the 3-dimensional Taylor-Goldstein equation numerically using hourly-averaged density and velocity profiles on November 9, 1991. We have shown that the sheared zone between the base of the surface mixed layer and the core of the EUC (the deep cycle layer) can exhibit dynamic instability. A thin shear layer at the lower edge of the EUC was also unstable.

For a complicated profile with several shear maxima, there can be multiple unstable modes with different critical levels. Each critical level is located at a local maximum of the reduced shear, $S-2N$. Therefore, observed wave signals at different depths could be due to different unstable modes.

The largest growth rate found in this study is $2.1 \times 10^{-3} \text{ s}^{-1}$, which corresponds to an e-fold growing time less than 8 minutes. The frequencies of these unstable modes are on the order of a few cph (Figure 2.10f), consistent with con-

current observations of interval waves. The propagation directions of these unstable modes are mostly zonal (Figure 2.10b, c, d, e), with phase speeds between -0.3 and 0.4 m s^{-1} . The wavelengths of instable modes range from 100 to 400 m (Figure 2.10g). These wavelengths are a few times the depth of the shear zone, as would be expected on the basis of simpler profiles (cf. section 4.2).

Our analysis is consistent with the scenario in which shear instability is responsible for the maintenance of the deep-cycle turbulence, as speculated by *Gregg et al.* [1985], *Peters et al.* [1989], *Moum et al.* [1992] and *McPhaden and Peters* [1992]. Small disturbances extract energy from the mean flow near the critical level through the interaction of Reynolds stress and mean shear. The kinetic energy is redistributed over large vertical extent, so that disturbances have significant amplitude far beyond the region of subcritical Richardson number. These unstable modes act to transfer momentum from the wind-driven near-surface flow to the lower flank of the Equatorial Undercurrent.

**3 PARAMETER DEPENDENCE OF SHEAR INSTABILITY UPON
BACKGROUND VARIABLES: RESULTS FROM LINEAR
STABILITY ANALYSIS**

Chaojiao Sun, William D. Smyth and James N. Moum
Oregon State University

To be submitted to *Journal of Fluid Mechanics*,
September 24, 1997.

3.1 Introduction

In the last chapter, we confirmed that ocean conditions typical of Equatorial Undercurrent (EUC) in the central Pacific were favorable to generation of strong shear instability. We numerically solved the linear stability problem using hourly-averaged profiles of velocity and density as background conditions, over a 24-hour period. Unstable modes with highest growth rates were found under nighttime background conditions. We concluded that shear instability could be a viable mechanism for the nighttime bursts of intense turbulence below the mixed layer, the so-called “deep cycle turbulence”.

If shear instability is responsible for the maintenance of the turbulence in the thermocline, the question immediately to be answered is: Is there a diurnal cycle in the growth rates of shear instability? We address this issue by analysis of linear stability of 5 consecutive days (about 120 profiles), including that day we studied in detail in the previous chapter.

Now that we have enough data points to study the statistics of unstable modes (a total of 144 unstable modes), we can investigate the explicit parameter dependence of shear instability waves upon the background variables. The goal is to be able to predict growth rate, as well as critical level, frequency and wavelength of unstable modes from the background conditions without solving the eigenvalue problem explicitly.

One of the primary goals of this paper is to determine the parameter dependence of the growth rates ω_i . Traditionally, gradient Richardson number ($Ri = N^2/S^2$, $N^2 = -g\rho_z/\rho$, $S^2 = U_z^2 + V_z^2$) is used for this purpose. The generation of shear instability is governed by the competing effects of destabilizing shear and stabilizing stratification. As we have noted in the previous chapter, Ri cannot

distinguish the cases when both S^2 and N^2 are large and both of them are small. It is clear that given the same (small) values of Ri , the former case is more unstable than the latter one. Here, we will propose a parameterization of growth rate based on the value of the reduced shear, $S - 2N$. In addition, we will show a remarkable correspondence of the critical levels and the depths of maxima of reduced shear (which coincide closely with the minima of Ri). It is shown that the propagation direction of instability waves roughly corresponds to the direction of shear vector at its critical levels. We also attempt to deduce the parameter dependence of the wavelengths of unstable modes upon the length scales of background flow.

In this chapter, our main goals are (1) to describe the temporal variability of dynamic instability over 5 consecutive days (section 3); (2) to determine the explicit parameter dependence of shear flow instability upon reduced shear, direction of shear vector at the critical levels, and other external (background) variables (section 4).

In section 3.2, we introduce the background conditions for the time period of our study. In section 3.3, the temporal variability of shear instability and the deep cycle of turbulence is discussed. In section 3.4, we test the hypotheses for parameterizations of characteristics of unstable modes. We present the conclusions in section 3.5.

3.2 Background conditions

The measurements were taken in 1991 during Tropical Instability Wave Experiments (TIWE), from November 7 (day 311) to November 11 (day 315).

During these five days, the maximum speed of the Equatorial Undercurrent (EUC) was about 0.8 m s^{-1} at around 120 m depth (Figure 3.1a). The semi-diurnal tidal signal was apparent in the zonal velocity. Meridional velocity was more variable

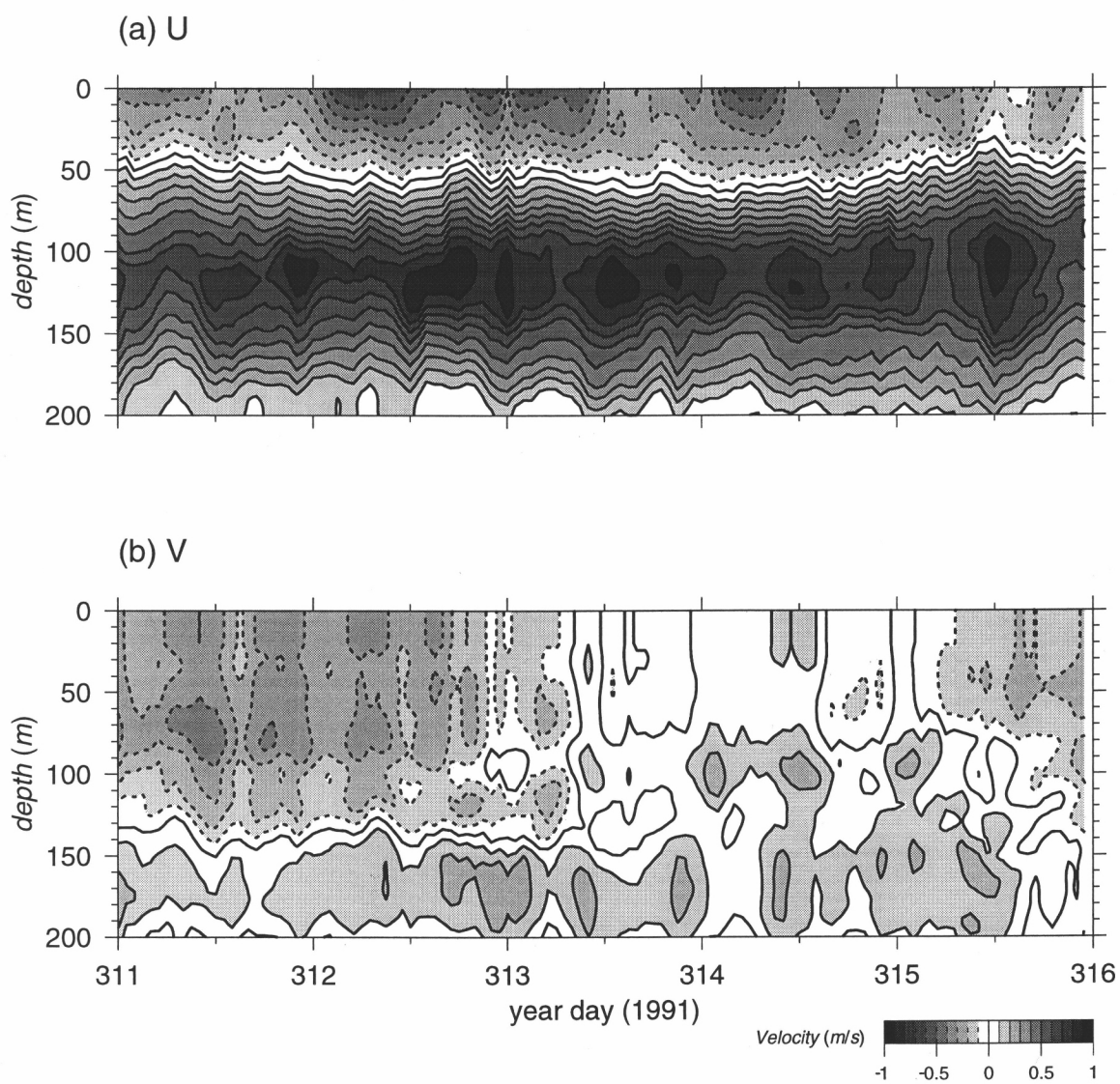


FIGURE 3.1. Hourly averaged (a) zonal (b) meridional velocity from day 311 to 315.

over this time period (Figure 3.1b). During the first two days (days 311 and 312) and about first 10 hours on the third day (day 313), meridional velocity was southward above 140 m with magnitude up to 0.5 m s^{-1} . But afterwards the southward flow disappeared until late day 314.

The vertical shear was dominated by its zonal component (Figure 3.2). The maximum shear in the zonal current was about 0.02 s^{-1} . Both zonal and meridional shear oscillated during these five days (Figure 3.2b). This oscillation was apparently associated with wind stress and large scale features in the ocean, such as advection and passage of large scale waves (Lien *et al.*, 1995).

N^2 was small above the thermocline at about 100 m depth (Figure 3.3a). It was largest from about 100 m to 160 m inside the core of the undercurrent. The thick black line superimposed on the image of N^2 was the location of the base of the surface mixed layer. The mixed layer depth was defined to be the depth at which the density exceeds surface value by 0.01 kg m^{-3} , following Peters *et al.* (1988) and Moum *et al.* (1989). It varied from 5 m to 15 m during daytime, and deepened to 20–40 m in the night.

The Richardson number was less than $1/4$ above the core of the EUC during most of the observation period (Figure 3.3b). Occasionally, Ri was also less than $1/4$ in the lower flank of the undercurrent, although over much smaller vertical extent. There is no diurnal cycle in Richardson number in the stratified layer below the mixed layer.

Figure 3.3c is an image and contour plot of reduced shear $S - 2N$. Positive values of reduced shear corresponds to $Ri < 1/4$. Reduced shear peaked during night and early morning hours. The peak values of $S - 2N$ became smaller on the last two days. We will show later this drop in $S - 2N$ resulted in weaker instability.

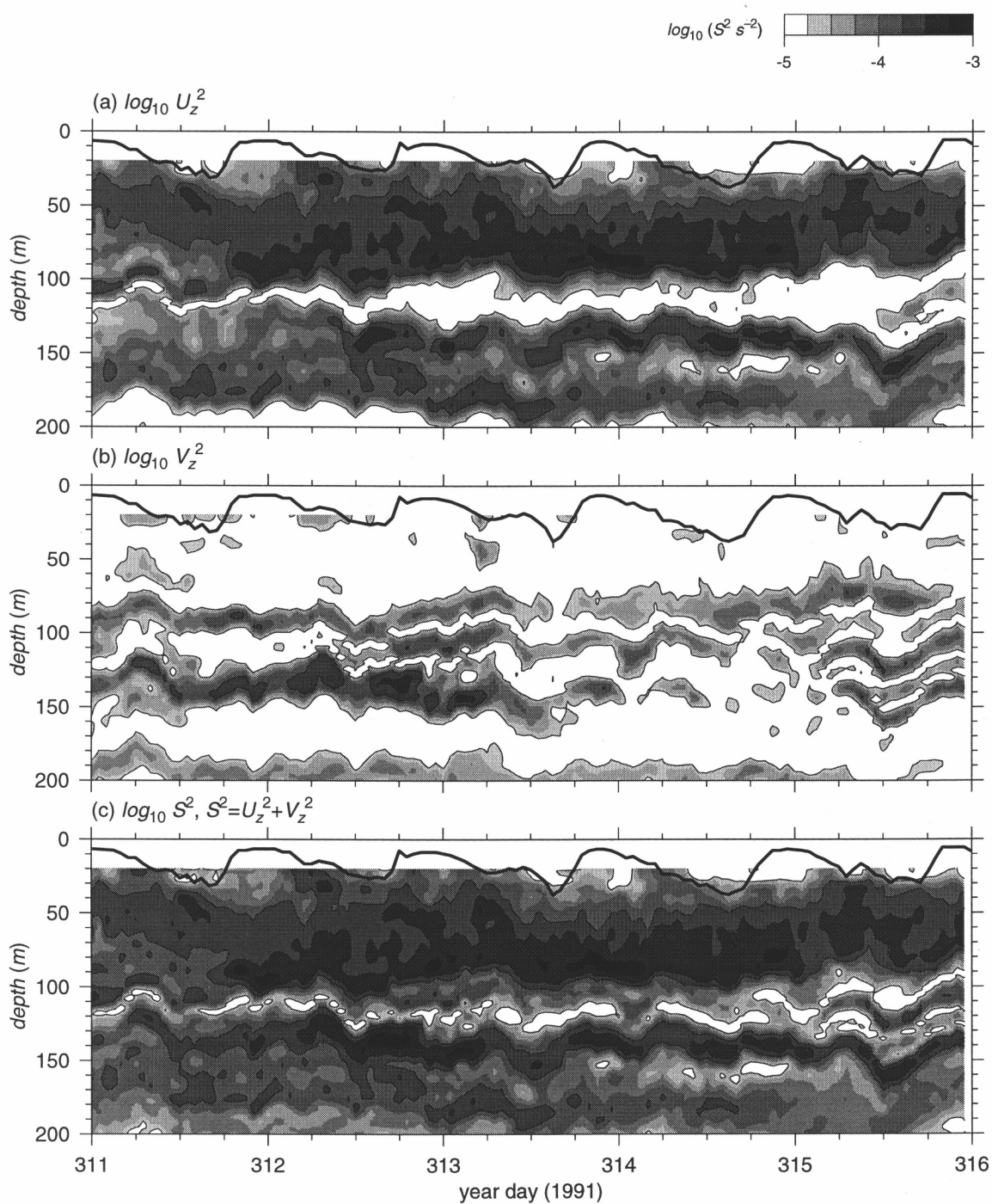


FIGURE 3.2. Squared hourly averaged (a) zonal shear (U_z^2) (b) meridional shear (V_z^2) (c) total shear ($U_z^2 + V_z^2$) from day 311 to 315. The thick black line denotes the base of the surface mixed layer.

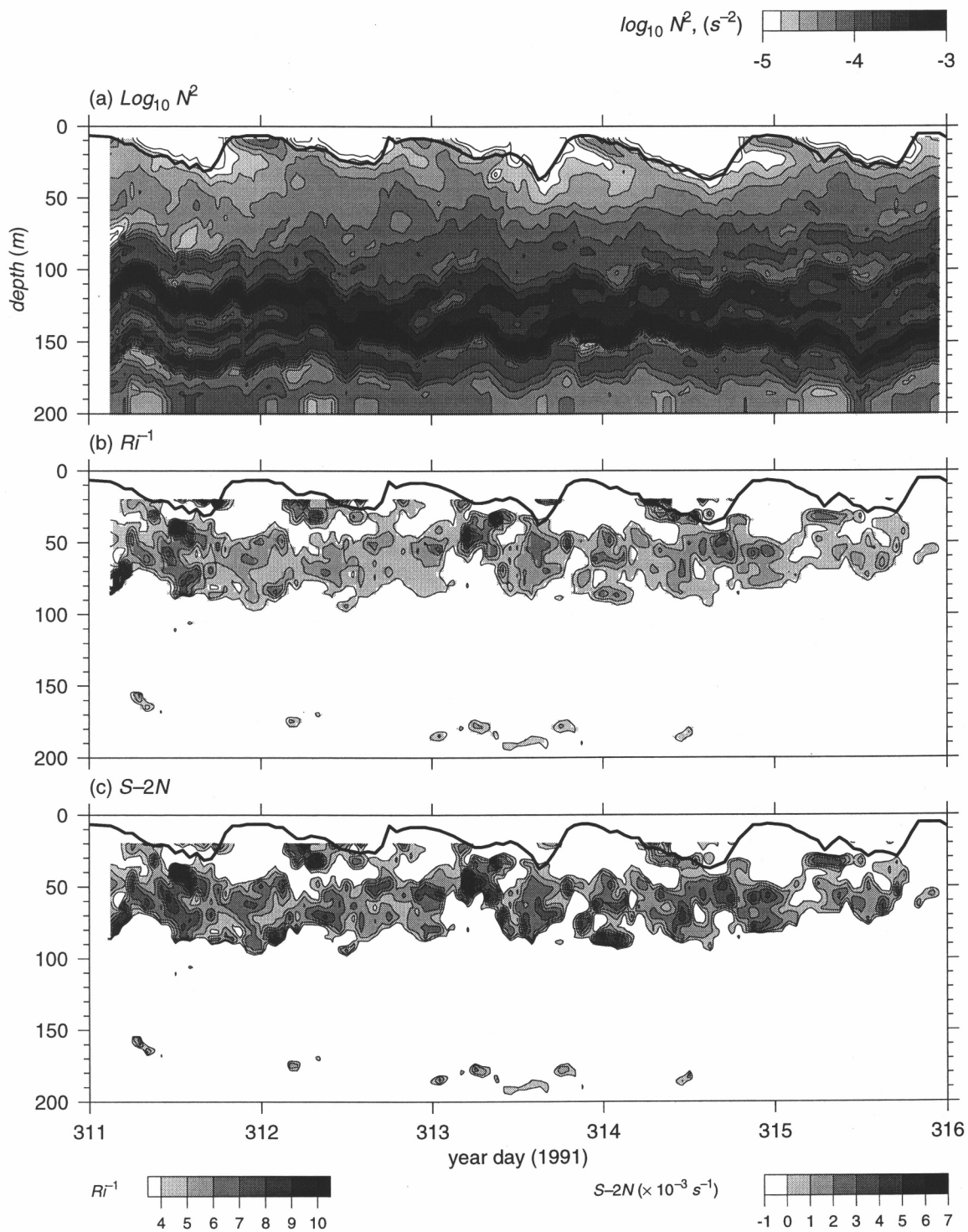


FIGURE 3.3. Hourly averaged (a) squared buoyancy frequency (N^2) (b) Inverse Richardson number (c) $S - 2N$ from day 311 to 315. The thick black line denotes the base of the surface mixed layer.

3.3 Variability of shear instability and deep cycle of turbulence

3.3.1 Variability of shear instability over 5 days

In this section, we investigate the variability in growth rates over this 5-day period. As discussed in Sun *et al.* (1997), the dispersion relation $\omega_i = \omega_i(k, l)$ exhibits a surface (possibly several overlapping surfaces) upon which the growth rate varies continuously. Each surface represents a continuum of unstable modes whose critical levels are close to a given depth. We refer to this continuum as a “family” of unstable modes. To simplify our discussions, we will refer to a mode family simply as “an unstable mode” as if it is a monochromatic mode, and use the parameters of the fastest growing mode (FGM) in the family for our discussions.

The critical levels of these unstable modes are distributed mostly in the deep-cycle zone with a few in a deep thin layer below the EUC (Figure 3.4). As in Sun *et al.* (1997), we organize the modes into four categories, based on the zonal current structure. We denote the shallow mode nearest to the surface as “mode 1” (squares in Figure 3.4)). Mode 1, by definition, has westward zonal phase velocity since the South Equatorial Current (SEC) was westward. On the boundary of between the SEC and the eastward-flowing EUC, the zonal velocity is almost zero. We refer to the modes with critical levels in this region as “mode 2” (triangles in Figure 3.4). The third class of modes have critical levels on the upper flank of the EUC, thus eastward phase velocity (bullets in Figure 3.4). The fourth mode resides in the thin layer on the lower flank of the undercurrent, near 180 m (diamonds in Figure 3.4).

We plotted the growth rates of unstable modes for each hour (Figure 3.5c). Strong instability occurred during the first three nights. The highest growth rate was about $2.1 \times 10^{-3} \text{ s}^{-1}$ (e-folding time ~ 8 minutes). The flow was less unstable on the last two days, with the highest value $6 \times 10^{-4} \text{ s}^{-1}$ (e-folding time ~ 28

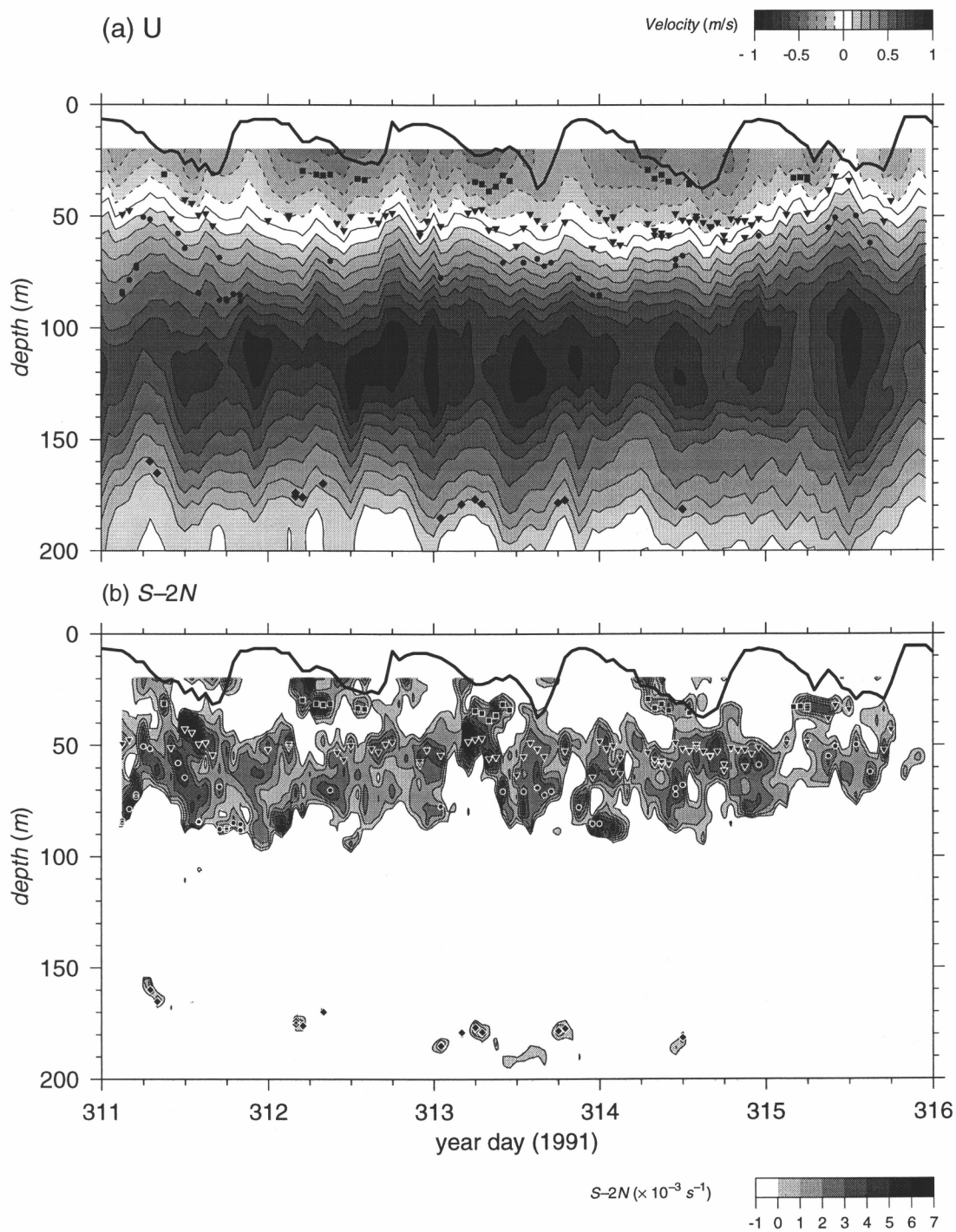


FIGURE 3.4. (a) Contours of zonal velocity U and (b) Reduced shear $S - 2N$. The thick black line in (a) and (b) denotes the base of the surface mixed layer. Different symbols in (a) and (b) represent different modes (box: mode 1; triangle: mode 2; bullet: mode 3; diamond: mode 4).

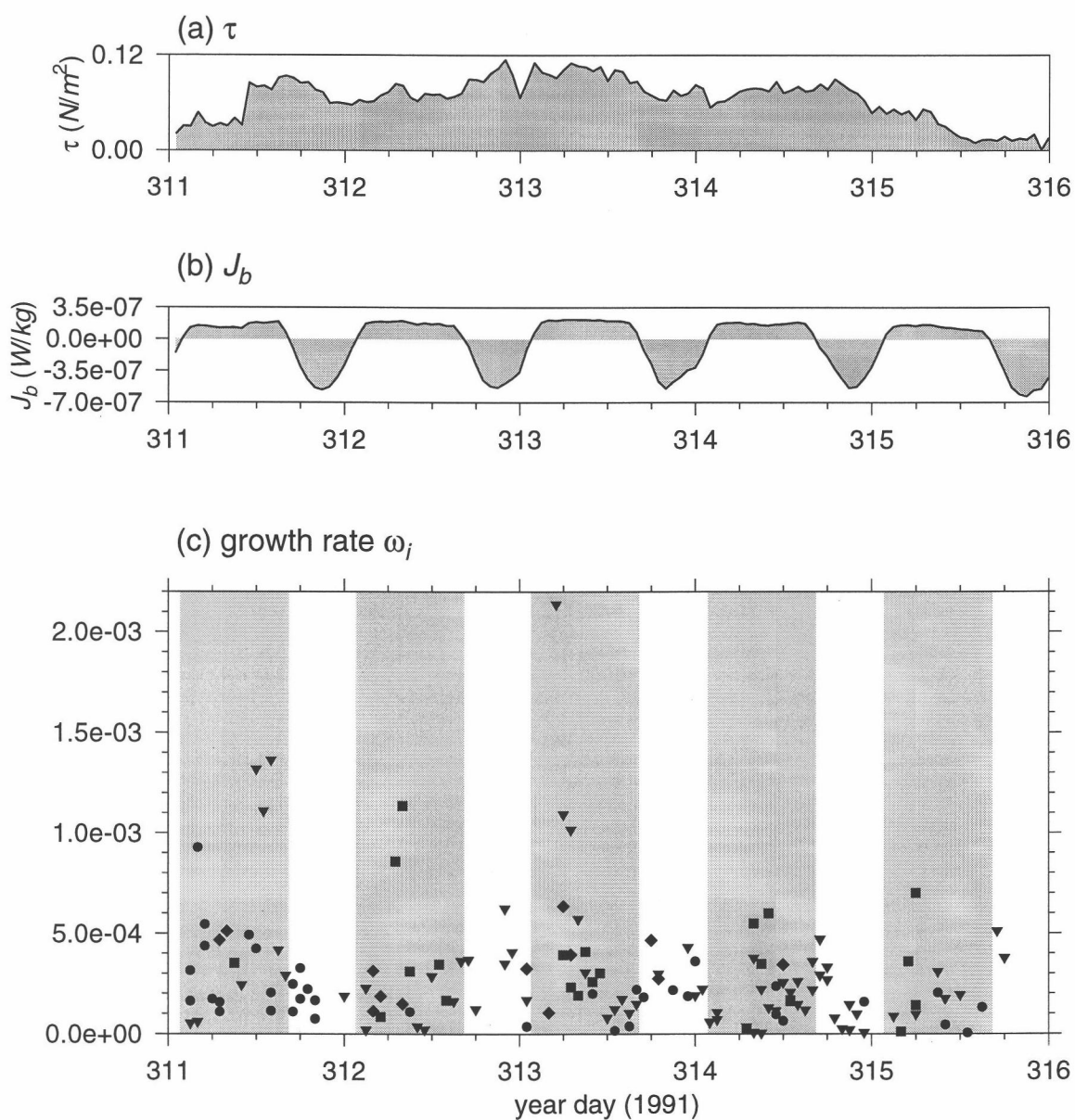


FIGURE 3.5. Time series of (a) wind stress τ (b) buoyancy flux J_b (c) growth rates of unstable modes ω_i . The shaded areas in (c) correspond to time periods when $J_b > 0$. Different symbols in (c) represent different modes (box: mode 1; triangle: mode 2; bullet: mode 3; diamond: mode 4).

minutes). The growth rates clearly exhibited diurnal variations. Strong instability occurred during nighttime everyday, although in the last two days the difference in the nighttime and daytime growth rates was smaller than in the previous days. This is probably due to weaker shear in the upper water column because of weak wind forcing.

The frequencies of these unstable modes are on the order of a few cycles per hour (cph) (Figure 3.6a). The wavelengths are between about 50 m and 600 m (Figure 3.6b). Most of the unstable modes have wavelengths in the range 100–400 m. The most energetic shear instability waves have a wavelength between about 100 to 300 m. This agrees with estimates from observations made from both Tropic Heat 2 and TIWE experiments (e.g., Moum *et al.*, 1992; McPhaden and Peters, 1992; Lien *et al.*, 1996; Levine and Moum, 1997).

3.3.2 Variability of the deep cycle of turbulence

In general, the turbulence in the deep-cycle zone was weak during the daytime, and strong during the nighttime. The intensity of turbulence was directly related to the wind forcing and surface heat flux (Figure 3.7). On the first day (day 311), the wind was initially weak and peaked up during the second half of the day. A patch of turbulence with high values of turbulent kinetic energy dissipation rate ϵ penetrated to as deep as 90 m. On the second day (day 312), the wind was weaker. The penetration depth of deep cycle was shallower and more intermittent. On the third day (day 313), the wind was the strongest in these five days. The turbulence was also the most energetic. The wind decreased on the fourth day, so did the turbulence. The wind eventually died down on day 315. ϵ in the deep cycle layer was smaller and only persisted for a short time.

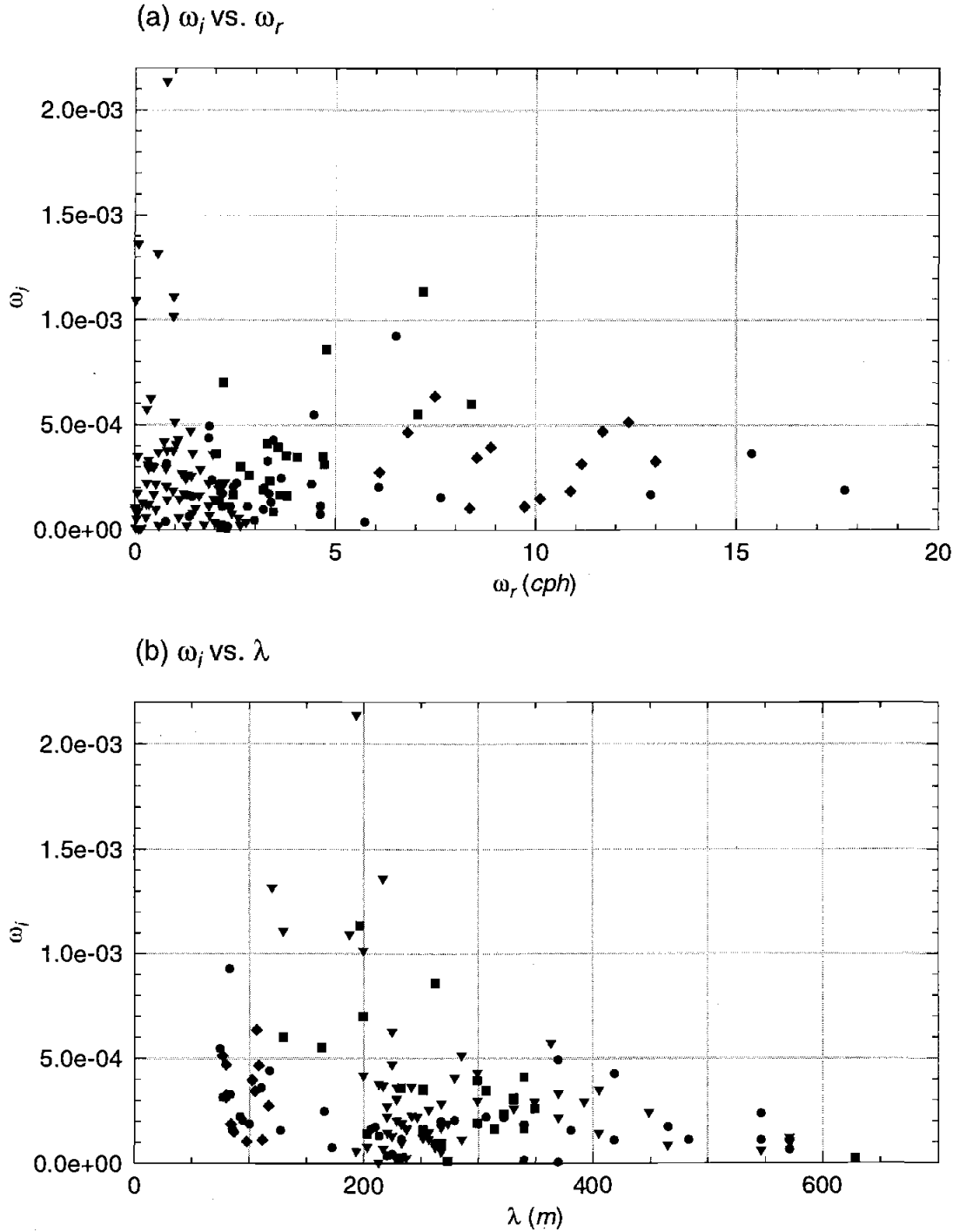


FIGURE 3.6. (a) Growth rates ω_i versus the Eulerian frequencies ω_r of unstable modes in the earth's frame. (b) Growth rates ω_i versus the wavelengths λ of the unstable modes. Different symbols in (a) and (b) represent different modes (box: mode 1; triangle: mode 2; bullet: mode 3; diamond: mode 4).

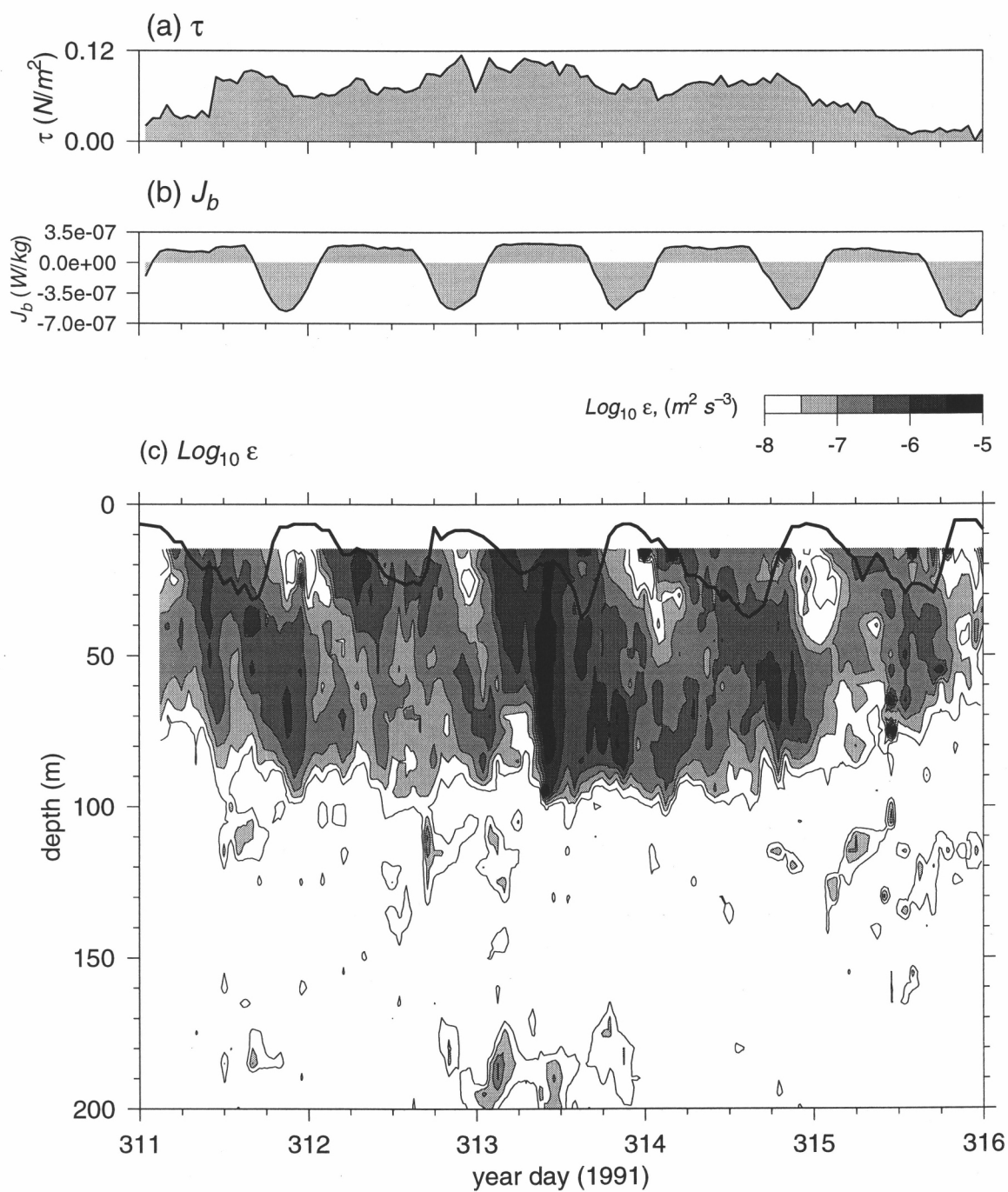


FIGURE 3.7. (a) wind stress τ . (b) buoyancy flux J_b . (c) Hourly averaged turbulent kinetic energy dissipation rate ϵ . The thick black line in (c) denotes the base of the mixed layer.

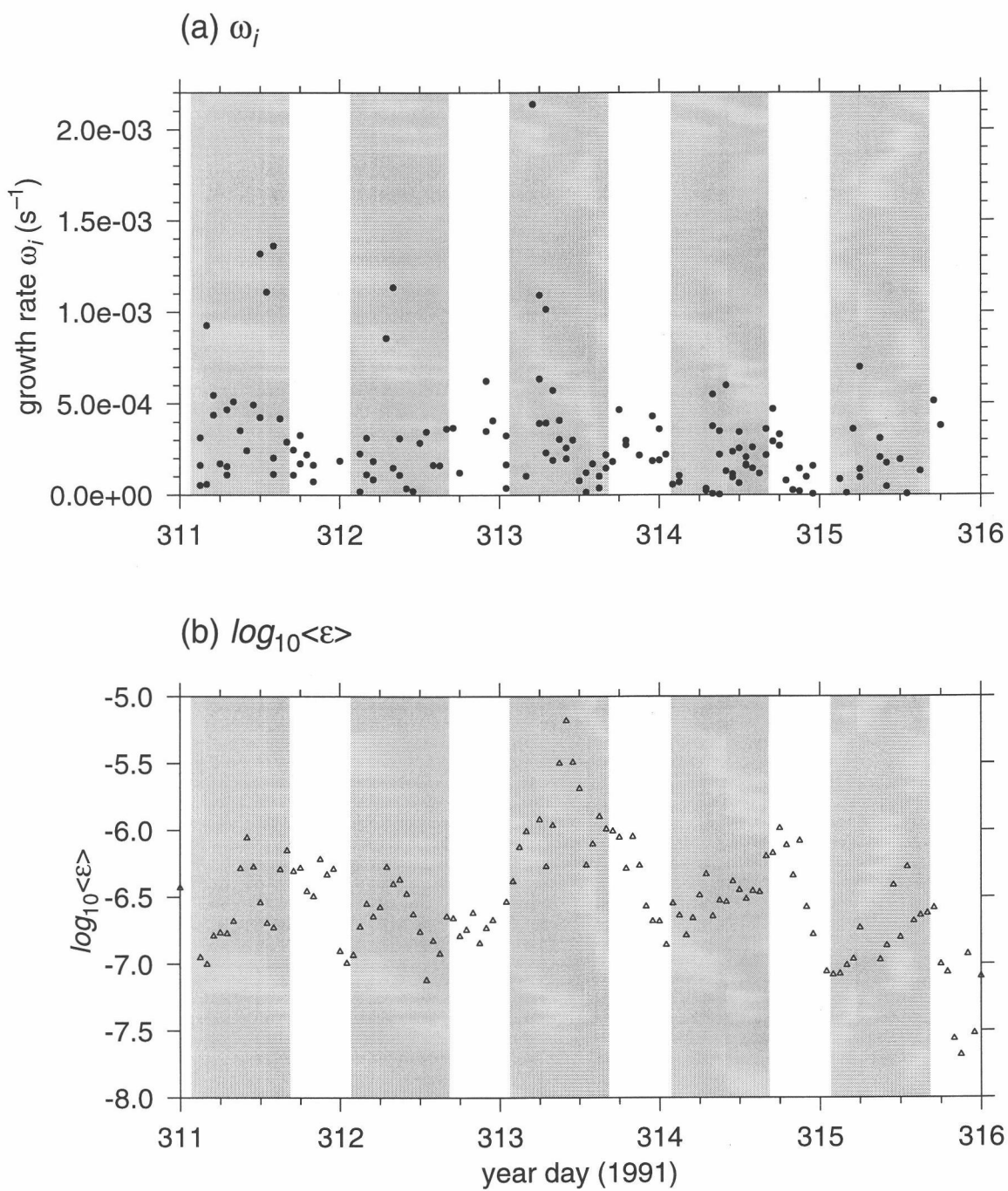


FIGURE 3.8. (a) Time series of growth rates. (b) Hourly averaged $\log_{10} \langle \epsilon \rangle$. $\langle \epsilon \rangle$ was averaged between the base of the mixed layer and the penetration depth of the deep cycle layer (taken here as 80 m depth). The shaded areas correspond to time periods when surface buoyancy flux $J_b > 0$.

High growth rates appeared to be corresponded with high values of ϵ averaged over the deep cycle layer (Figure 3.8). High ϵ usually occurred in the night. So did the high growth rates. The highest ϵ ($10^{-5} \text{ m}^2 \text{ s}^{-3}$) occurred two hours after the onset of the most energetic shear instability (growth rate = $2.2 \times 10^{-3} \text{ s}^{-1}$). This suggests that shear instability could be a very important source for the generation of the deep cycle of turbulence in this region. We do not have an exact one-to-one correspondence between the growth rates and ϵ . It is possible that there is a mismatch in the space-time resolution of measured ϵ and computed growth rates. Processes other than shear instability could also have been playing a role in the dynamics of the deep-cycle region.

3.4 Parameter dependence of instability

In this section, we examine a set of parameters of unstable modes and investigate how they are related to the parameters of background profiles. The four parameters of unstable modes we study are growth rate, critical level, wavelength and propagation direction.

To evaluate the significance of the correlation between a parameter of unstable modes and that of the background, we use the Spearman correlation coefficient r_s (Press *et al.*, 1992).

3.4.1 What determines the location of critical level?

As in Sun *et al.* (1997), we find that the critical level of each unstable mode is close to the depth of the nearest local Ri minimum (Figure 3.9a). The rms deviation (z_{rms}) is about 2 m. They are almost perfectly correlated (the Spearman correlation coefficient is 0.97). We find the similar Spearman correlation coefficient

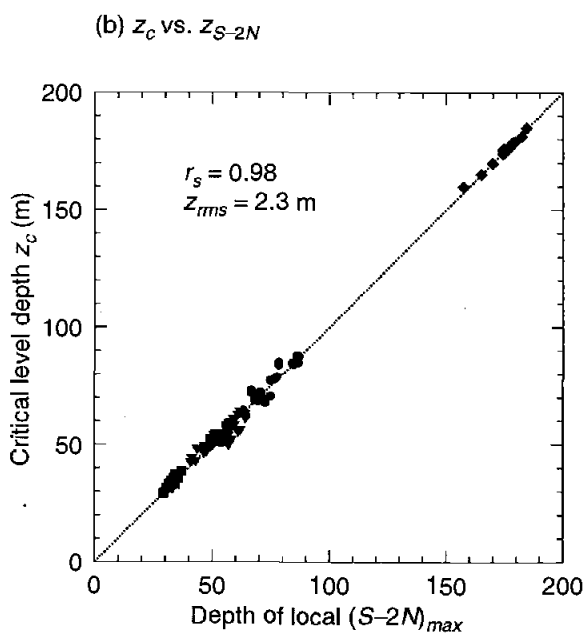
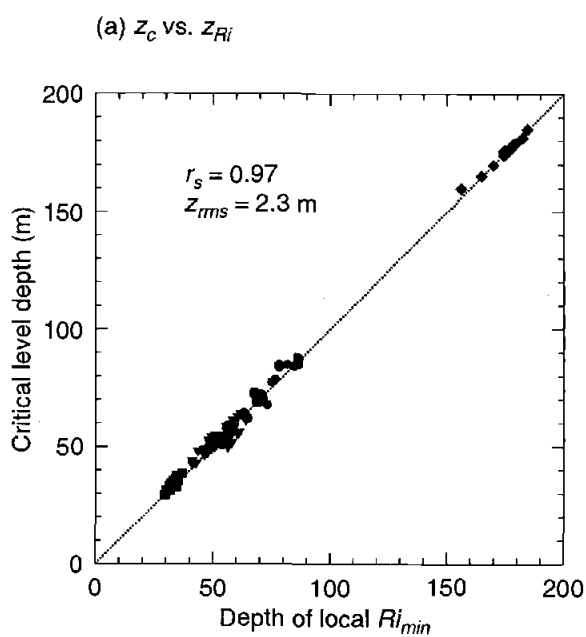


FIGURE 3.9. (a) Critical level depth (z_c) versus the depth of local Richardson number minimum (z_{Ri}). z_{rms} is the *rms* different between z_c and z_{Ri} . (b) Critical level depth (z_c) versus the depth of local $S - 2N$ maximum (z_{S-2N}). z_{rms} is the *rms* different between z_c and z_{S-2N} . r_s is the Spearman rank correlation coefficient. Different symbols in (a) and (b) represent different modes (box: mode 1; triangle: mode 2; bullet: mode 3; diamond: mode 4).

(0.98) between the critical level and local $S - 2N$ maximum (Figure 3.9b). The rms deviation between these two variables is also about 2 m. It is no surprise since the depth of local maximum of $S - 2N$ is closely correlated with the depth of local Ri minimum (Figure 3.10a). ($r_s = 1.00$, $z_{rms} = 0.5$ m.)

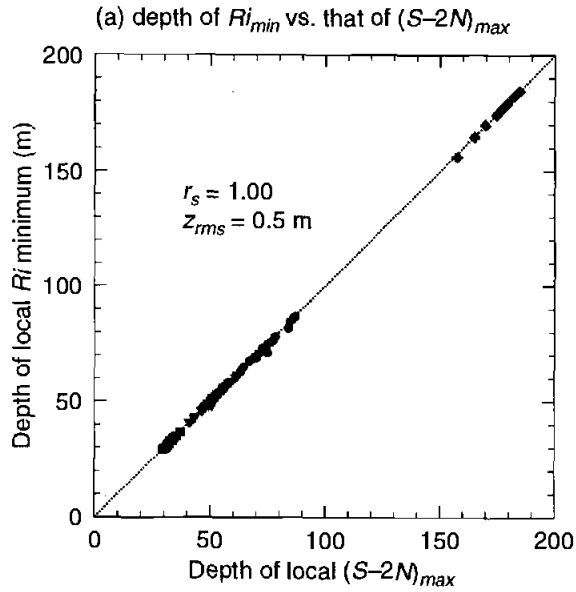
The critical levels for the majority of unstable modes (about 91%) are in the range of 30–100 m, which is within the depth range of the deep-cycle layer. 9% of unstable modes have critical levels between 150 and 180 m, which is beneath the core of EUC and the thermocline.

3.4.2 What determines the growth rate?

Others have found that growth rate normalized by shear is correlated with the Ri at the critical level. In this study, the growth rate normalized by the shear is found to be negatively correlated with the gradient Richardson number (both S and Ri are evaluated at the critical level). The smaller the Ri , the larger the normalized growth rates (Figure 3.10b). The Spearman coefficient is -0.48.

Kunze *et al.* (1990) examined the results of Hazel (1972) for hyperbolic tangent background profiles and found that growth rates of the fastest growing modes were proportional to reduced shear ($S - 2N$). They showed that $(S - 2N)/4$ (both S and N are evaluated at the depth of Ri minimum) was a good estimator of the maximum growth rates when Ri is less than 0.125.

Because the unstable modes in our calculations were from a variety of background profiles, the flow geometry was complicated. We cannot expect the relationship found by Kunze *et al.* (1990) between growth rate ω_i and reduced shear $S - 2N$ to hold exactly for the cases studied here. Assuming that the growth rate



(b) ω_l/S vs. Ri

$$y = (0.070 \pm 0.090) + (-0.319 \pm 0.001) * x$$

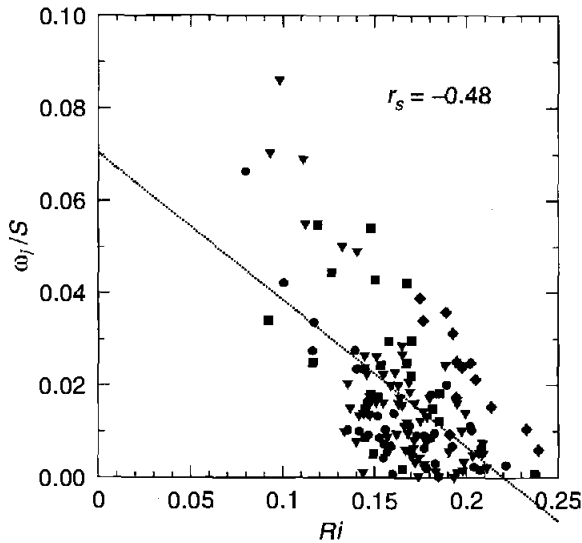


FIGURE 3.10. (a) The depth of local Richardson number minimum (z_{Ri}) versus the depth of local $S - 2N$ maximum (z_{S-2N}). z_{rms} is the *rms* different between z_{Ri} and z_{S-2N} . (b) Growth rate normalized by the shear at its critical level versus the Richardson number at the critical level. r_s is the Spearman rank correlation coefficient. Different symbols in (a) and (b) represent different modes (box: mode 1; triangle: mode 2; bullet: mode 3; diamond: mode 4).

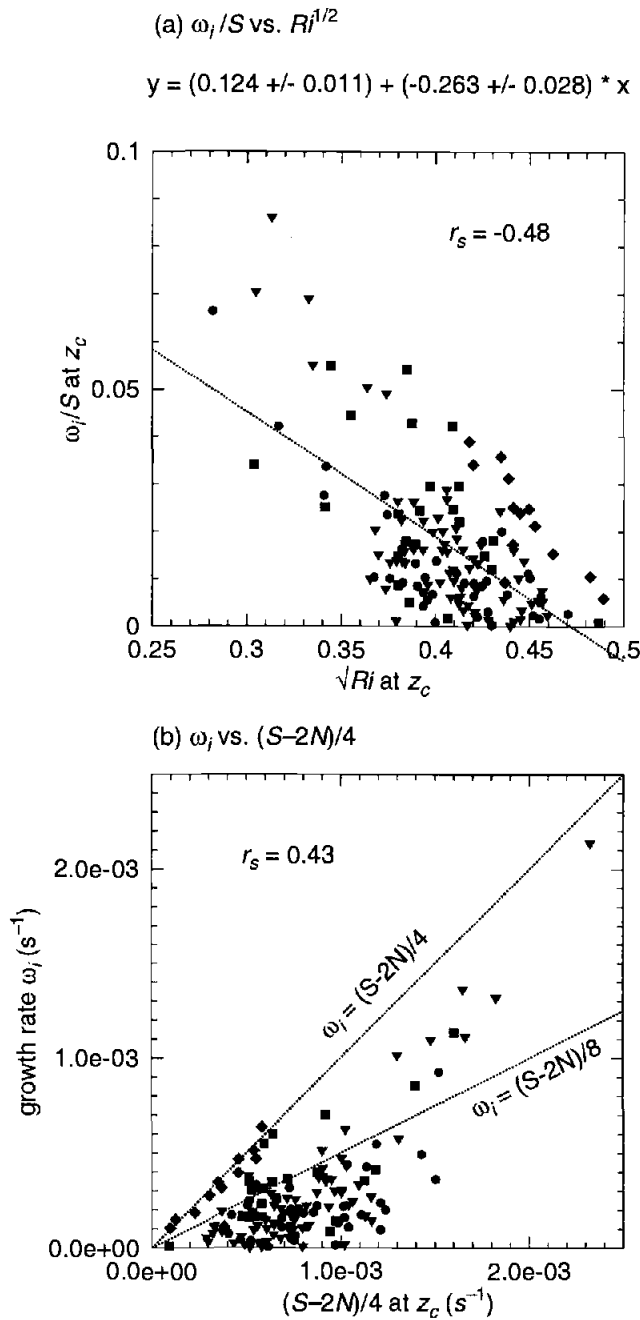


FIGURE 3.11. (a) Normalized growth rate ω_i/S versus \sqrt{Ri} evaluated at the critical level. (b) Growth rate ω_i versus $(S - 2N)/4$ evaluated at the critical level. r_s is the Spearman rank correlation coefficient. Different symbols in (a) and (b) represent different modes (box: mode 1; triangle: mode 2; bullet: mode 3; diamond: mode 4).

of instability is proportional to a linear combination of S and N ,

$$\omega_i = aS - bN,$$

where a and b are unknown constants, we try to determine a and b from statistical analysis.

Since

$$\frac{\omega_i}{S} = \frac{aS - bN}{S} = a - b\sqrt{Ri},$$

the linear regression of ω_i/S vs. \sqrt{Ri} provides the constants a and b . The regression yields $a = 0.124$, and $b = 0.263$ (Figure 3.11a). The standard deviations of a and b are 0.011 and 0.030, respectively. This gives the relationship between growth rate and reduced shear

$$\omega_i \simeq 0.125(S - 2N).$$

This suggests that on the average, the growth rate of unstable modes for complex ocean profiles is smaller by a factor of 2 than those for *tanh* profiles.

The growth rate and $(S - 2N)/4$ (both S and N evaluated at the critical level) are positively correlated with correlation coefficient 0.47 (Figure 3.11b). $(S - 2N)/4$ appears to be the upper bound on the growth rates for more complicated profiles studied here. This seems to suggest that hyperbolic tangent profiles may be the most efficient profiles for shear instability to grow. The average value of growth rate is approximated by a half of $(S - 2N)/4$ in the least square sense.

To understand the differences from Kunze *et al.* (1990), we try to determine different relations between growth rates and reduced shear for different background profiles. We analyzed Hazel's results for different background functions in the same fashion as Kunze *et al.* (1990) did. We will study the relationship between maximum growth rates of different profiles and the various background parameters evaluated at the Ri minimum. The squares in Figure (3.12 and 3.13) are from hyperbolic tangent

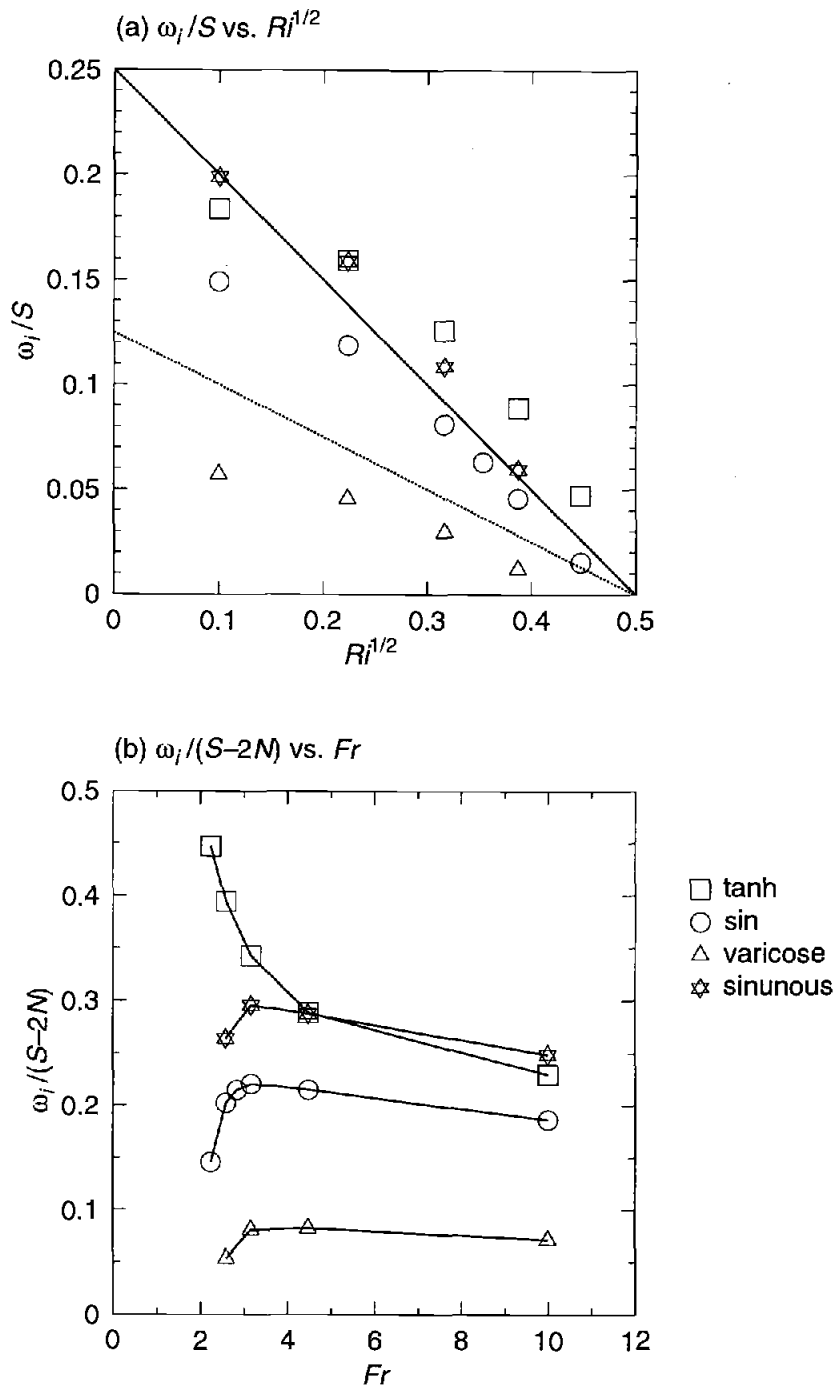


FIGURE 3.12. (a) ω_i/S vs. \sqrt{Ri} for the *tanh*, *sin* and *sech*² functions, which corresponds to the prototypes of smooth shear layer, channel flow and Bickley jet. (From Hazel, 1972, Figures 1, 14 and 17.) (b) $\omega_i/(S-2N)$ vs. Fr for the same set of functions as in (a). ($Fr = S/N = 1/\sqrt{Ri}$.)

profiles (Figure 1 in Hazel). The circles are from the channel profiles, $u(z) = \sin(z)$ (Figure 14 in Hazel). The triangles and stars are from the varicose and sinuous modes of the Bickley jet, respectively (Figure 17 in Hazel).

In Figure (3.12a), The solid line is $\omega_i/S = 0.25(S - 2N)$, the dashed line is $\omega_i/S = 0.125(S - 2N)$. It appears that $\omega_i/S \simeq 0.25(S - 2N)$ is a good approximation except for the varicose mode. Kunze *et al.* (1990) based their conclusion on a plot like Figure (3.12b), which suggested that, the ratio $\omega_i/(S - 2N)$ tends to be constant for $Fr > 3$ (Fr is the Froude number, $Fr = S/N$), which corresponds to $\sqrt{Ri} < 0.33$, but with different values for different functions. The ratio is about 0.25 for \tanh profile and sinuous modes for the Bickley jet, about 0.2 for \sin profiles, and about 0.8 for the varicose mode of the Bickley jet. Therefore the scattering in Figure (3.11a) may be explained in two ways: the background profiles have different function shapes, and the majority of unstable modes have $\sqrt{Ri} > 0.33$.

Similar information is obtained by plotting the ratio $\omega_i/(S - 2N)$ vs. Ri (Figure 3.13a). Now we see clearly that $\omega_i/(S - 2N)$ stays nearly constant for all the modes except \tanh modes. For modes from \tanh profiles and the sinuous modes from Bickley jet, the maximum growth rate of unstable modes are slightly higher than $(S - 2N)/4$ (Figure 3.13b). ω_i is slightly smaller than $(S - 2N)/4$ for unstable modes of \sin profile. It is much smaller than $(S - 2N)/4$ for the varicose modes of the Bickley jet.

In short, we find that growth rate normalized by shear may be parameterized by Ri (both shear S and Ri are evaluated at the critical level). In other words, growth rate may be parameterized by SRi . The combination of Ri and magnitude of shear, not just the Ri , may diagnose the instability. Similar is the case between growth rate and reduced shear, since reduced shear is another way of combining the information of Ri and the magnitude of shear, $S - 2N = S(1 - 2/\sqrt{Ri})$.

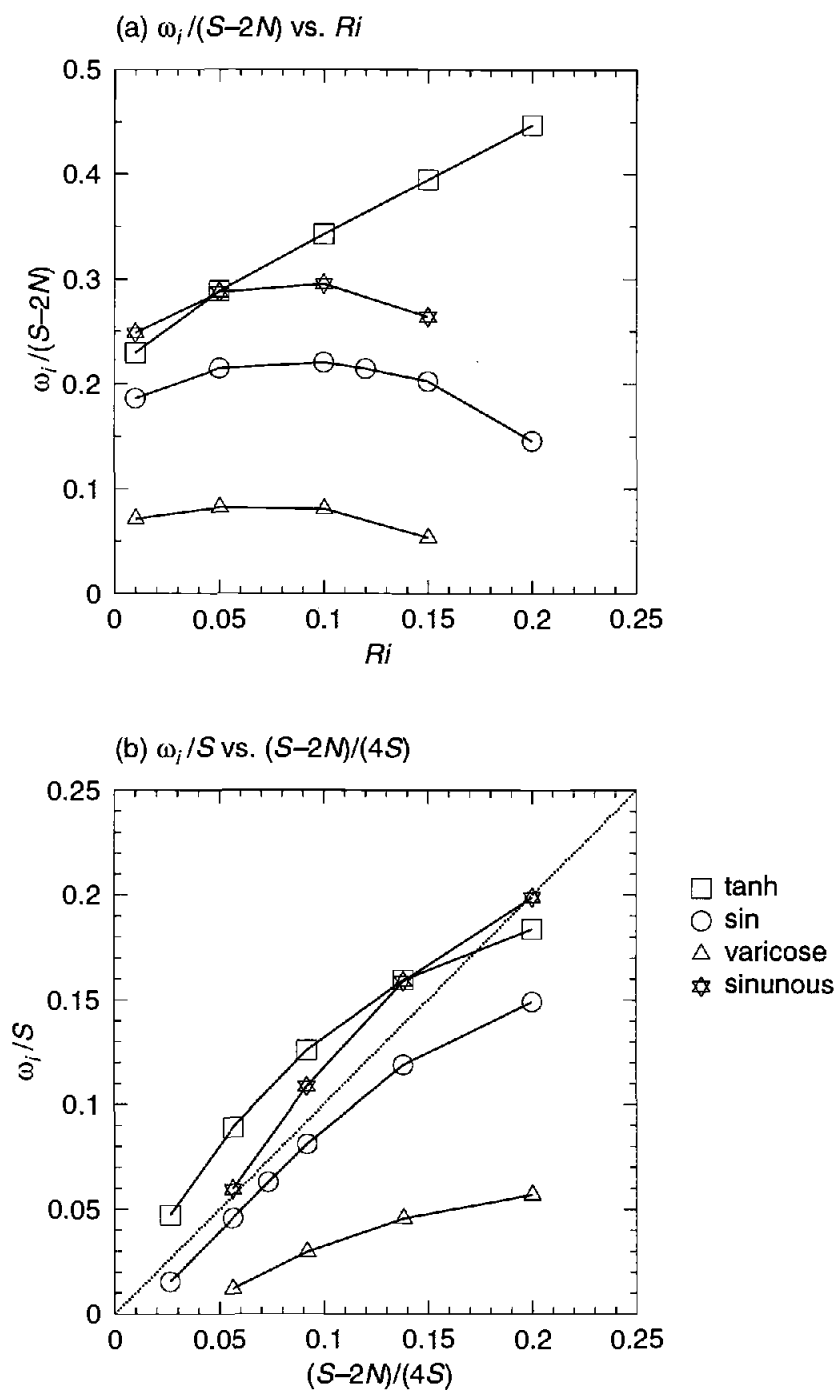


FIGURE 3.13. (a) ω_i/S vs. Ri for *tanh*, *sin* and *sech* functions, which corresponds to the prototype of smooth shear layer, channel flow and Bickley jet. (b) ω_i/S vs. $(S-2N)/(4S)$. The data points are extracted from Hazel (1972).

Based on our knowledge of the relationship about locations of the critical level in 3.4.1, we can provide the following recipe for estimating the growth rate. Find the local maxima of positive reduced shear (or local minima of $Ri < 1/4$). Those are the approximate locations of the critical levels. Then compute $S - 2N$ for each critical level. The growth rate is approximately $(S - 2N)/4$.

3.4.3 What determines the propagation direction?

Now we test the hypothesis that an unstable mode should propagate in the direction of the maximum shear, i.e., either along or against the direction of the shear vector at its critical level (θ_S), since that is the direction of largest reduced shear, and the smallest Ri . Because our prediction of θ_F is uncertain by an additive constant of 180° , we rectify θ_F and θ_S to lie in the range $(-90^\circ, 90^\circ)$. The direction of the FGM (θ_F) is plotted against the direction of maximum shear at the critical level in Figure 3.14a. They are highly correlated with Spearman correlation coefficient 0.82. The standard deviation between θ_F and θ_S is about 12° . This is a reasonably good agreement considering the factor of the range of propagation directions of a mode family.

The propagation direction of an unstable mode is somewhat difficult to define exactly. Due to three dimensionality of the dispersion relations, the growth rate of the FGM of a mode family may not be significantly larger than its neighboring modes, which are spreading away from the direction of the FGM. It is therefore misleading to think that the direction of the FGM were determined exactly in these calculations. The neighboring modes with growth rates within 90% of the maximum growth rate of the FGM are usually distributed in a range of directions. The average value for such a range is about 10° .

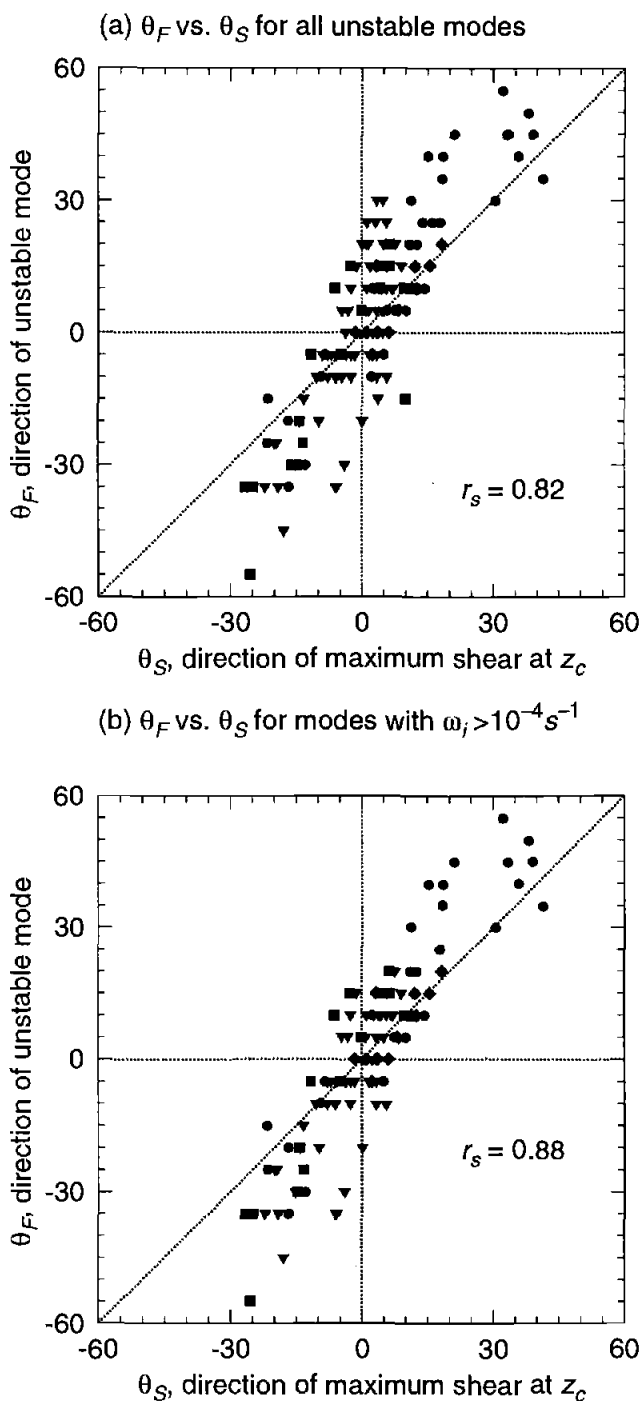


FIGURE 3.14. (a) Direction of unstable modes versus the direction of maximum shear at the critical level (144 modes). (b) Same as in (a) except only for modes with growth rates $\omega_i > 10^{-4} s^{-1}$. r_s is the Spearman rank correlation coefficient. Different symbols in (a) and (b) represent different modes (box: mode 1; triangle: mode 2; bullet: mode 3; diamond: mode 4).

There appears to be a trend for the direction of unstable modes to deviate away from the direction of maximized shear so that (θ_F) has larger angles from the zonal direction than θ_S . We cannot determine the cause of this trend. Excluding those modes with tiny growth rates ($\omega_i > 10^{-4} s^{-1}$), which we suspect may be subject to numerical inaccuracy, we are left with 114 modes (79% of all the modes). This improves the Spearman correlation coefficient slightly to 0.88 (Figure 3.14b). The standard deviation between θ_F and θ_S is about 11° . So the trend is not due to errors introduced by modes with small growth rates.

3.4.4 What determines the wavelength?

For a hyperbolic tangent profile, the wavelength of the fastest growing instability ranges from 4 to 8 times the shear-layer depth (e.g., Drazin, 1958; Miles and Howard, 1964; Davis and Peltier, 1976). The so-called shear-layer depth is defined as the depth over which the current shear is large. Since there is no such well-defined “shear layer” in our profiles, we attempt to find a relevant parameter to determine the wavelength.

Since reduced shear is the most important parameter in diagnosing shear instability, we suspect the radius of curvature of reduced shear at the critical level, R_{S-2N} , is the relevant parameter. We also investigated the possible role of the radius of curvature of the gradient Richardson number at the critical level, R_{Ri} .

The wavelength is correlated with the curvature of radius of reduced shear, R_{S-2N} , with a Spearman rank-correlation coefficient 0.45 (Figure 3.15a). It is correlated with that of gradient Richardson number, R_{Ri} , with a smaller Spearman rank-correlation coefficient, 0.38 (Figure 3.15b). Assuming that the wavelength λ is proportional to R_{S-2N} , the least-square fit is $\lambda = 24R_{S-2N}$. The fit between λ

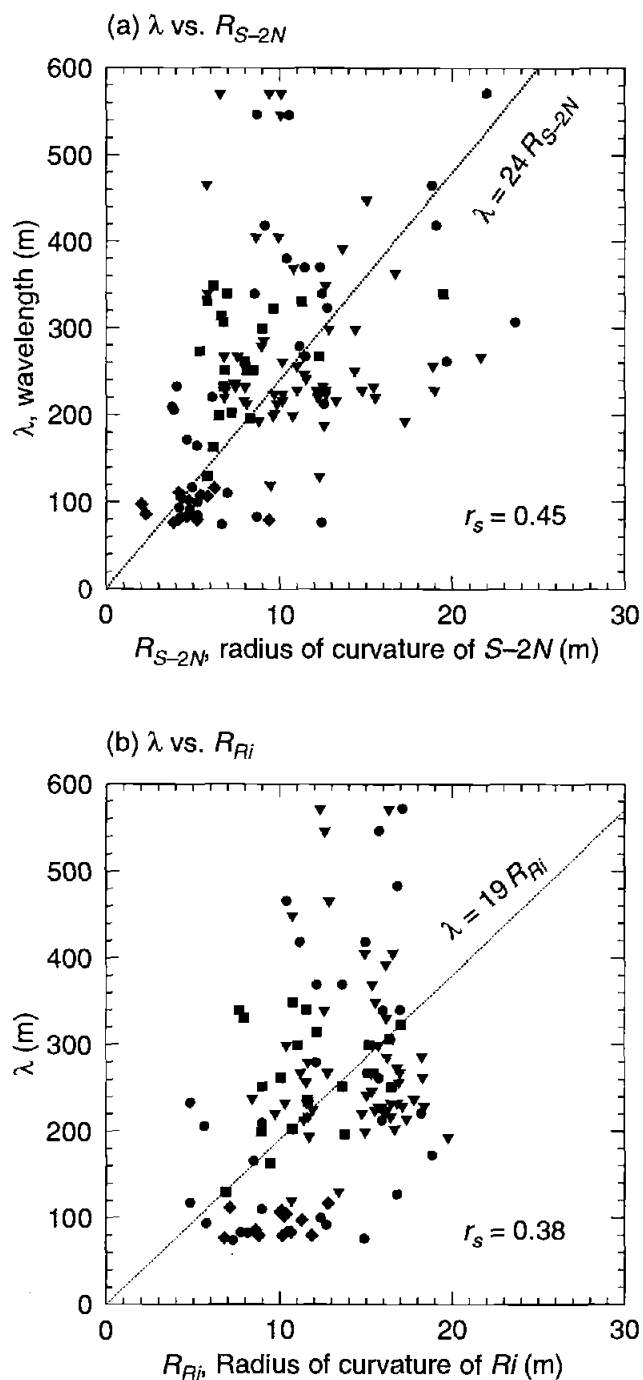


FIGURE 3.15. (a) Wavelengths of unstable modes λ versus R_{S-2N} , the radius of curvature of $S - 2N$ at the critical level. (b) Wavelengths λ versus R_{Ri} , the radius of curvature of Ri at the critical level. r_s is the Spearman rank correlation coefficient. Different symbols in (a) and (b) represent different modes (box: mode 1; triangle: mode 2; bullet: mode 3; diamond: mode 4).

and the radius of curvature of the gradient Richardson number at the critical level, R_{Ri} , is $\lambda = 19R_{Ri}$.

3.5 Conclusions

A diurnal cycle in the intensity of shear instability is clearly seen from the numerical solutions of stability problem of five days of continuous data. The strongest instability occurred during the nighttime. Its occurrence was closely related to the outburst of intense turbulence in the deep cycle layer. This supports the idea that shear instability is responsible for the maintenance of deep-cycle turbulence.

The parameter dependence of the characteristics of unstable modes upon the the background variables is investigated. Reduced shear ($S - 2N$) is an important parameter in diagnosing shear instability, because it takes into account the magnitude of the shear, while Ri is just a ratio of shear over stratification. It has been used successfully in parameterizations of turbulent production rate in shear-driven turbulence (Kunze *et al.*, 1990; Polzin *et al.*, 1995; Polzin, 1996). The growth rate of unstable modes may be parameterized by the reduced shear (evaluated at the critical level). $(S - 2N)/4$ appears to be an upper bound for the growth rate of shear instability. This agrees with the conclusion of Kunze *et al.* (1990). Moreover, the average growth rate of unstable modes is approximately $(S - 2N)/8$, a factor of 2 smaller than the upper bound.

The critical level of unstable waves is located near the location of local maximum of reduced shear ($S - 2N$), which is close to the location of local minimum of Ri . Most of unstable modes have critical levels in the deep-cycle layer between about 30 and 100 m. However, a substantial number of unstable modes were associated with the lower flank of the equatorial Undercurrent at 150–180 m depth.

Shear instability waves tend to propagate along (or against) the direction of the shear vector at its critical level. This is intuitively correct since this is the direction along which the available mean shear is the maximum. The wavelength of shear instability waves is approximately proportional to the radius of curvature of reduced shear at the critical level.

4 GENERAL CONCLUSIONS

The discovery of deep-cycle turbulence in the Central Equatorial Pacific was made during the Tropic Heat experiments in 1984 and 1987. The turbulent kinetic energy dissipation rate (ϵ) in the stratified region below the mixed layer increased by at least one order of magnitude in the nighttime than during the day. This phenomenon has important implications for the vertical redistribution of momentum in the upper equatorial ocean.

What is the source of the turbulence in this deep cycle region which is not directly influenced by the surface forcing? It has been speculated that the enhanced turbulence at night in this region could be due to growing shear instability waves, because the gradient Richardson number (Ri) there was close to a critical value of $1/4$ for instability to occur. The reasoning was that when internal waves generated elsewhere 0 into this region, the additional wave shear could reduce the Ri below $1/4$. As a consequence, shear instability could occur.

However, $Ri < 1/4$ is a necessary but insufficient condition for instability to occur. Even if Ri is well below $1/4$, there is no guarantee that shear instability will occur. Previous numerical and laboratory studies usually dealt with simple shear layer condition. Those results might not be applicable to the complicated profiles in the ocean.

During Tropical Heat Wave Experiment (TIWE) in the central Equatorial Pacific in 1991, the Richardson number was constantly below $1/4$ in the deep-cycle layer. This provides us the opportunity to study the stability problem numerically with these measurements. We try to answer the following questions: was realistic ocean condition capable of generating shear instability? If so, what is the time scale

of the growth of shear instability? Is there a diurnal cycle in the growth rates of shear instability?

- We have shown that realistic ocean conditions favored nighttime instability generation with high growth rates. There is a diurnal cycle in the growth rates of shear instability. The high growth rates corresponded to enhanced turbulence in the deep-cycle layer. Therefore shear instability is a valid mechanism for the generation of deep-cycle turbulence.

- There exist radiating unstable modes, thus providing a mechanism for the vertical transfer of momentum and heat from the upper ocean into the interior ocean. This conclusion could have important implications for closing the momentum balance in the upper equatorial ocean.

- The mechanism through which an unstable mode extracts energy from the mean flow is via the interaction of Reynolds stress and mean current shear at its critical level. The extracted energy is redistributed away from the critical level by the vertical energy flux. Thus shear instability waves are not limited to small- Ri region, as previously believed.

- For a complicated background profile with several local Ri minima, there are possibly several unstable modes, each with its critical level located at the depth of the nearest local Ri minimum. This may explain why there are patches of turbulence at different depths.

From extended stability analysis using five days of continuous data (about 120 profiles), we examined the statistics of the parameters of unstable modes and how they are related to the parameters of background conditions. The goal is to be able to predict the potential importance of shear instability for a given background condition without numerically solving the stability problem. We found that the parameters of unstable modes, including the growth rate, critical level, wave-

length, and propagation direction, are significantly correlated to the parameters of background conditions.

- The critical level of unstable waves is located near the depth of local maximum of reduced shear ($S - 2N$), which is close to the depth of local minimum of Ri . Most of unstable modes have critical levels in the deep-cycle layer between about 30 and 100 m. The critical levels of the rest of them are below the thermocline.

- The growth rate of shear instability is approximately proportional to reduced shear ($S - 2N$, both S and N are evaluated at the critical level). $(S - 2N)/4$ appears to be an upper bound. The average growth rate of unstable modes is about $(S - 2N)/8$, a factor of 2 smaller than the upper bound. We thus propose to use reduced shear $S - 2N$ to predict the possibility of instability, instead of the gradient Richardson number Ri .

- The shear instability wave tends to propagate along the direction of maximum shear at its critical level. This is intuitively correct since the amount of energy available from the mean flow is largest along that direction.

- The most energetic shear instability waves have a wavelength between about 100 to 300 m. This agrees with the estimates from observations. The wavelength of shear instability waves is approximately proportional to the radius of curvature of reduced shear at the critical level.

BIBLIOGRAPHY

- [1] Booker, J. R., and F. P. Bretherton, 1967: The critical layer for internal gravity waves in a shear flow. *J. Fluid Mech.*, **27**, 513–539.
- [2] Boyd, T.J., D. S. Luther, R. A. Knox, and M. C. Hendershott, 1993: High-frequency internal waves in the strongly sheared currents of the upper equatorial Pacific: Observations and a simple spectral model. *J. Geophys. Res.*, **98**, 18,089–18107.
- [3] Davis, P. A. and W. R. Peltier, 1976: Resonant parallel shear instability in the stably stratified planetary boundary layer. *J. Atmos. Sci.*, **33**, 1287–1300.
- [4] De Bass, A. F. and A. G. M. Driedonks, 1985: Internal gravity waves in a stably stratified boundary layer. *Boundary-Layer Meteorol.*, **31**, 303–323.
- [5] Drazin, P.G., 1958: The stability of a shear layer in an unbounded heterogeneous inviscid fluid. *J. Fluid Mech.*, **4**, 214–224.
- [6] Hebert, D., J. N. Moum, C. A. Paulson, and D. R. Caldwell, 1992: Turbulence and internal waves at the equator. Part II: Details of a single event. *J. Phys. Oceanogr.*, **22**, 1346–1356.
- [7] Howard, L. N., 1961: Note on a paper of John W. Miles. *J. Fluid Mech.*, **10**, 509–512.
- [8] Howard, L. N. and S. A. Maslowe, 1973: Stability of stratified shear flows. *Boundary-Layer Meteorol.*, **4**, 511–523.
- [9] Kunze, E., A. J. Williams, and M. G. Briscoe, 1990: Observations of shear and vertical stability from a neutrally buoyant float. *J. Geophys. Res.*, **95**, 18,127–18,142.
- [10] Levine, M. D., and J. N. Moum, 1997: Detailed observations of an equatorial internal wave packet. *J. Phys. Oceanogr.*, manuscript to be submitted.
- [11] Lien, R.-C., M. McPhaden, and D. Hebert, 1994: Intercomparison of ADCP measurements at 0, 140W. *J. Atmos. Oceanic Technol.*, **11**, 1334–1349.
- [12] Lien, R.-C., D. R. Caldwell, M. C. Gregg, and J. N. Moum, 1995: Turbulence variability at the equator in the central Pacific at the beginning of the 1991–1993 El Niño. *J. Geophys. Res.*, **100**, 6881–6898.
- [13] Lien, R.-C., M. McPhaden, and M. C. Gregg, 1996: High-frequency internal waves at 0°, 140°W and their possible relationship to deep-cycle turbulence. *J. Phys. Oceanogr.*, **26**, 581–600.

- [14] Lott, F., H. Kelder, and H. Teitelbaum, 1992: A transition from Kelvin–Helmholtz instabilities to propagating wave instabilities. *Phys. Fluids A*, **4**, 1990–1997.
- [15] Mack, A. P., and D. Hebert, 1997: Internal gravity waves in the Upper Eastern Equatorial Pacific: Observations and numerical solutions. *J. Geophys. Res.*, manuscript submitted.
- [16] McPhaden, M. J., and H. Peters, 1992: On the diurnal cycle of internal wave variability in the equatorial Pacific Ocean: Results from moored observations. *J. Phys. Oceanogr.*, **22**, 1317–1329.
- [17] Miles, J. W., 1961: On the stability of heterogenous shear flows. *J. Fluid Mech.*, **10**, 496–508.
- [18] Miles, J. W. and L. N. Howard, 1964: Note on a heterogeneous shear flow. *J. Fluid Mech.*, **20**, 331–336.
- [19] Moum, J. N., and D. R. Caldwell, 1985: Local influences on shear flow turbulence in the equatorial ocean. *Science*, **230**, 315–316.
- [20] Moum, J. N., D. R. Caldwell, and C. A. Paulson, 1989: Mixing in the equatorial surface layer and thermocline. *J. Geophys. Res.*, **94**, 2,005–2021.
- [21] Moum, J. N., M. J. McPhaden, D. Hebert, H. Peters, C. A. Paulson, and D. R. Caldwell, 1992a: Internal waves, dynamic instabilities, and turbulence in the equatorial thermocline: an introduction to three papers in this issue. *J. Phys. Oceanogr.*, **22**, 1357–1359.
- [22] Moum, J. N., D. Hebert, C. A. Paulson and D. R. Caldwell, 1992b: Turbulence and internal waves at the equator. Part I: Statistics from towed thermistors and a microstructure profiler. *J. Phys. Oceanogr.*, **22**, 1330–1345.
- [23] Moum, J. N., M. C. Gregg, R. C. Lien and M. E. Carr, 1995: Comparison of turbulent kinetic energy dissipation rates from two ocean microstructure profilers. *J. Atmos. Oceanic. Technol.*, **12**, 346–366.
- [24] Pedlosky, J., 1987: *Geophysical Fluid Dynamics*. Springer–Verlag, New York.
- [25] Peters, H., M. C. Gregg, and J. M. Toole, 1988: On the parameterization of equatorial turbulence. *J. Geophys. Res.*, **93**, 1199–1218.
- [26] Peters, H., M. C. Gregg, and J. M. Toole, 1989: Meridional variability of turbulence through the equatorial undercurrent. *J. Geophys. Res.*, **94**, 18003–18009.
- [27] Polzin, K. L., J. M. Toole, and R. W. Schmitt, 1995: Finescale parameterizations of turbulent dissipation. *J. Phys. Oceanogr.*, **25**, 306–328.

- [28] Polzin, K. L., 1996: Statistics of the Richardson number: mixing models and finestructure. *J. Phys. Oceanogr.*, **26**, 1409–1425.
- [29] Press, W. H., , S. A. Teukolsky, W. T. Vetterling and B. P. Flannery, 1992: Numerical Recipes. 2nd edition. Cambridge.
- [30] Skillingstad, E. D., and D. W. Denbo, 1994: The role of internal gravity waves in the Equatorial current system. *J. Phys. Oceanogr.*, **24**, 2093–2110.
- [31] Smyth, W. D., and W. R. Peltier, 1989: The transition between Kelvin–Helmholtz instability: an investigation of the overreflection hypothesis. *J. Atmos. Sci.*, **46**, 3698–3720.
- [32] Sun, C., W. D. Smyth, and J. N. Moum, 1997: Parameterization of shear instability waves by the Richardson number. *J. Fluid Mech.*, manuscript to be submitted.
- [33] Sutherland, B. R., and W. R. Peltier, 1992: The stability of stratified jets. *Geophys. Astrophys. Fluid Dynamics*, **66**, 101–131.
- [34] Sutherland, B. R., 1996: Dynamic excitation of internal gravity waves in the equatorial ocean. *J. Phys. Oceanogr.*, **26**, 2398–2419.
- [35] Wijesekera, H. W., and T. M. Dillon, 1991: Internal waves and mixing in the upper equatorial Pacific Ocean. *J. Geophys. Res.*, **96**, 7115–7126.
- [36] Winters, K. B., and J. J. Riley, 1992: Instability of internal waves near a critical level. *Dynamics of Atmospheres and Oceans*, **16**, 249–278.

APPENDICES

APPENDIX A Derivation of 3-D Taylor–Goldstein equation

For an inviscid, incompressible, stratified, shear flow, making the Boussinesq approximation, we get the following set of linear equations

$$u'_t + Uu'_x + Vu'_y + w'U_z = -p'_x \quad (\text{A1})$$

$$v'_t + Uv'_x + Vv'_y + w'V_z = -p'_y \quad (\text{A2})$$

$$w'_t + Uw'_x + Vw'_y = -g\rho' - p'_z \quad (\text{A3})$$

$$u'_x + v'_y + w'_z = 0 \quad (\text{A4})$$

$$\rho'_t + U\rho'_x + V\rho'_y + w'\bar{\rho}_z = 0 \quad (\text{A5})$$

where $\mathbf{u}' = (u', v', w')$ is the perturbation velocity in Cartesian coordinates. Subscripts x , y , z , and t denote differentiation. $\mathbf{U}(z) = (U(z), V(z), 0)$ and $U(z)$ and $V(z)$ represent mean velocity components in the zonal and meridional directions, respectively. ρ_0 is the reference density, taken as a constant value representing an averaged density value for the whole water column. $\bar{\rho}(z)$ is the undisturbed mean density field. $\rho'(x, y, z, t)$ is the perturbation density normalized by the reference density, $\rho' = (\rho - \bar{\rho}(z))/\rho_0$. p' is the perturbation pressure divided by the reference density ρ_0 .

Perturbation eigenfunctions $\hat{u}(z)$, $\hat{v}(z)$, $\hat{p}(z)$, $\hat{\rho}(z)$ can be expressed in terms of $\hat{w}(z)$ using the polarization relations:

$$\hat{u} = -i\frac{l}{\kappa^2\sigma}(lU_z - kV_z)\hat{w} + i\frac{k}{\kappa^2}\hat{w}_z \quad (\text{A6})$$

$$\hat{v} = i\frac{k}{\kappa^2\sigma}(lU_z - kV_z)\hat{w} + i\frac{l}{\kappa^2}\hat{w}_z \quad (\text{A7})$$

$$\hat{\rho} = i\frac{N^2}{g\sigma}\hat{w} \quad (\text{A8})$$

$$\hat{p} = i\frac{1}{\kappa^2}(lV_z + kU_z)\hat{w} + i\frac{\sigma}{\kappa^2}\hat{w}_z \quad (\text{A9})$$

where N is the local buoyancy frequency, defined by $N^2(z) = -g\bar{\rho}_z/\rho_0$. $\sigma = \omega - \mathbf{U} \cdot \mathbf{K}$ is the Doppler-shifted complex frequency.

The Taylor–Goldstein equation (2.2) is now obtained by substituting (A6) and (A7) into (2.3).

APPENDIX B The radiation boundary condition and its effects

So that waves generated at the shear layer can propagate downward into the thermocline, a radiation boundary condition is imposed at the lower boundary:

$$\hat{w}_z = im\hat{w} \quad \text{at } z = -D \quad (\text{B1})$$

where

$$m = \pm \sqrt{\frac{N^2}{(\tilde{U} - c)^2} + \frac{\tilde{U}_{zz}}{(\tilde{U} - c)} - \kappa^2} \quad (\text{B2})$$

the sign is chosen so that the vertical kinetic energy flux at the lower boundary (averaged over one horizontal wavelength) is directed downward, i.e.

$$\overline{p'w'} = \frac{|\hat{w}|^2}{2\kappa} \text{Re}\{m(\tilde{U} - c)\} < 0 \quad \text{at } z = -D$$

This is equivalent to

$$\text{Re}\{m(\tilde{U} - c)\} < 0, \quad \text{at } z = -D. \quad (\text{B3})$$

With rigid boundary conditions imposed at both horizontal boundaries, there are some well-documented properties of the solutions of the Taylor–Goldstein equation. For example, if there exists a solution with eigenvalue c and eigenfunction w , then eigenvalue c^* and eigenfunction \hat{w}^* are also solutions to the Taylor–Goldstein equation and rigid boundary conditions [e.g., *Hazel*, 1972]. The Miles–Howard theorem states that if Richardson number is greater than 1/4 everywhere in the flow, then the flow field is linearly stable, i.e., infinitesimal disturbances will not grow exponentially with time [*Miles*, 1961; *Howard*, 1961]. Howard’s semi-circle theorem provides a useful bound on the complex phase velocity of an unstable mode [*Howard*, 1961]. However, it is not immediately clear what the effects of radiation boundary condition are on these properties, and we consider this further here.

When the impermeable condition, $\hat{w} = 0$, is imposed at both boundaries, and an eigenvalue solution exists with complex phase speed c , then there is also a mode with phase speed c^* , i.e., every growing mode is accompanied by a decaying mode, and vice versa [e.g., *Hazel*, 1972]. Here we will show that the radiation condition upsets this symmetry by introducing a preference for decaying modes.

Assume a solution of Taylor–Goldstein equation (2.2) and boundary conditions with the complex phase speed c_1 , the corresponding eigenfunction is \hat{w}_1 . Do eigenvalue $c_2 = c_1^*$, and eigenfunction $\hat{w}_2 = \hat{w}_1^*$ satisfy radiation condition at the lower boundary.

Specifically, we want to investigate whether the vertical flux of perturbation kinetic energy $\overline{p_2' w_2'} = (1/2)\text{Re}\{\hat{p}_2 \hat{w}_2^*\}$ will be downward at the lower boundary $z = -D$.

From polarization relation (A9),

$$\hat{p}_2 = -\hat{p}_1^* \quad (\text{B4})$$

Therefore,

$$\overline{p_2' w_2'} = \frac{1}{2}\text{Re}\{\hat{p}_2 \hat{w}_2^*\} = \frac{1}{2}\text{Re}\{-\hat{p}_1^* \hat{w}_1\} = -\overline{p_1' w_1'} > 0$$

So radiation boundary condition cannot be satisfied with the complex conjugate solution. The complex conjugate symmetry in the solutions is no longer valid with the radiation condition.

The Howard semi-circle theorem with radiation boundary condition at the lower boundary and impermeable boundary condition at the upper boundary becomes [*De Bass and Driedonks*, 1985]

$$\left[c_r - \frac{1}{2}(\tilde{U}_{min} + \tilde{U}_{max}) \right]^2 + c_i^2 \leq \frac{1}{4}(\tilde{U}_{min} - \tilde{U}_{max})^2 - \frac{\int_0^0 N^2 |F|^2 dz}{\int_{-D}^0 Q dz} \quad (\text{B5})$$

where $F = \hat{w}/(\tilde{U} - c)$, and $Q = |F_z|^2 + \kappa^2|F|^2 > 0$.

The second term on the right-hand side of (B5) represents the modification due to the radiation condition. The new term has the effect of shrinking the semi-circle within which instability is possible. Unfortunately, the new term involves the eigenfunction, so it cannot be used to sharpen the *a priori* bounds on unstable eigenvalues. However, we can conclude that the original semicircle theorem remains valid when the radiation condition is applied.

It was shown by *Miles* [1961] and *Howard* [1961] that, under rigid boundary conditions, the flow is stable to disturbances of small amplitude, if the Richardson number $Ri = N^2/(U_z^2 + V_z^2)$ is everywhere larger than a critical value $1/4$. The effective Richardson number $\tilde{R}i = N^2/\tilde{U}_z^2$ is based on the vertical gradient of the component of the basic flow parallel to the horizontal wavenumber. $\tilde{R}i$ is always larger than or equal to the Richardson number Ri [*Booker and Bretherton*, 1967]. For a specific direction θ , if the effective Richardson number $\tilde{R}i$ is greater than $1/4$ everywhere, then the flow is stable to disturbances that propagate in that direction.

Here we will show that Miles–Howard theorem remains valid in the presence of a radiation boundary condition, i.e., Richardson number Ri smaller than $1/4$ at some depth is still a necessary condition for shear instability.

Similar to the proof of Miles–Howard theorem by *Howard* [1961], let us define a new variable ϕ by

$$\phi = \frac{\hat{w}}{\sqrt{\tilde{U} - c}} \quad (\text{B6})$$

With the new variable ϕ , the Taylor–Goldstein equation becomes

$$\{(\tilde{U} - c)\phi_z\}_z - \left\{ \kappa^2(\tilde{U} - c) + \frac{1}{2}\tilde{U}_{zz} + \frac{\frac{1}{4}\tilde{U}_z^2 - N^2}{(\tilde{U} - c)} \right\} \phi = 0 \quad (\text{B7})$$

The boundary conditions are

$$\phi = 0 \text{ at } z = 0 \quad (\text{B8})$$

$$\phi_z = im\phi - \frac{\tilde{U}_z}{2(\tilde{U} - c)}\phi \text{ at } z = -D \quad (\text{B9})$$

Now multiply B7 by the complex conjugate of ϕ , ϕ^* , integrate from $z = -D$ to $z = 0$, and take the imaginary part:

$$c_i \int_{-D}^0 \left\{ \frac{N^2 - \frac{1}{4}\tilde{U}_z^2}{|\tilde{U} - c|^2} |\phi|^2 + |\phi_z|^2 + \kappa^2 |\phi|^2 \right\} dz = \text{Re}\{m(\tilde{U}(-D) - c)\} |\phi(-D)|^2 \quad (\text{B10})$$

If $N^2 > \frac{1}{4}\tilde{U}_z^2$ everywhere in the basic flow, then the integral on the left hand side is positive, while the right hand side of the equation is negative due to the radiation boundary condition (B3). We thus conclude that c_i must be negative. Therefore, linear stability of the flow field is guaranteed if the Richardson number $Ri > 1/4$ everywhere in the flow, just as in the case of impermeable boundaries.

The effects of the radiation condition on the validity of the Miles–Howard and semicircle theorem are intuitively reasonable. Because the radiation condition only allows perturbation energy to be removed from the domain, its presence tends to stabilize the flow. Therefore, in regions of parameter space where the flow is demonstrably stable in the presence of rigid boundaries, the flow will remain stable when outgoing radiation is allowed.